Title: A large-scale optogenetic neurophysiology platform for improving accessibility in NHP behavioral experiments

Authors

- Devon J. Griggs 1, 2
- Julien Bloch 2, 3
- Noah Stanis 2, 3
- Jasmine Zhou 2, 3
- Shawn Fisher 1, 2
- Hesamoddin Jahanian 4
- Azadeh Yazdan-Shahmorad 1, 2, 3, 5 *

Affiliations

- 1 University of Washington, Seattle, Department of Electrical and Computer Engineering
- 2 Washington National Primate Research Center
- 3 University of Washington, Seattle, Department of Bioengineering
- 4 University of Washington, Seattle, Department of Radiology
- 5 Weill Neurohub
- * Corresponding author

Abstract

Optogenetics has been a powerful scientific tool for two decades, yet its integration with non-human primate (NHP) electrophysiology has been limited due to several technical challenges. These include a lack of electrode arrays capable of supporting large-scale and long-term optical access, inaccessible viral vector delivery methods for transfection of large regions of cortex, a paucity of hardware designed for large-scale patterned cortical illumination, and inflexible designs for multi-modal experimentation. To address these gaps, we introduce a highly accessible platform integrating optogenetics and electrophysiology for behavioral and neural modulation with neurophysiological recording in NHPs. We employed this platform in two rhesus macaques and showcased its capability of optogenetically disrupting reaches, while simultaneously monitoring ongoing electrocorticography activity underlying the stimulation-induced behavioral changes. The platform exhibits long-term stability and functionality, thereby facilitating large-scale electrophysiology, optical imaging, and optogenetics over months, which is crucial for translationally relevant multi-modal studies of neurological and neuropsychiatric disorders.

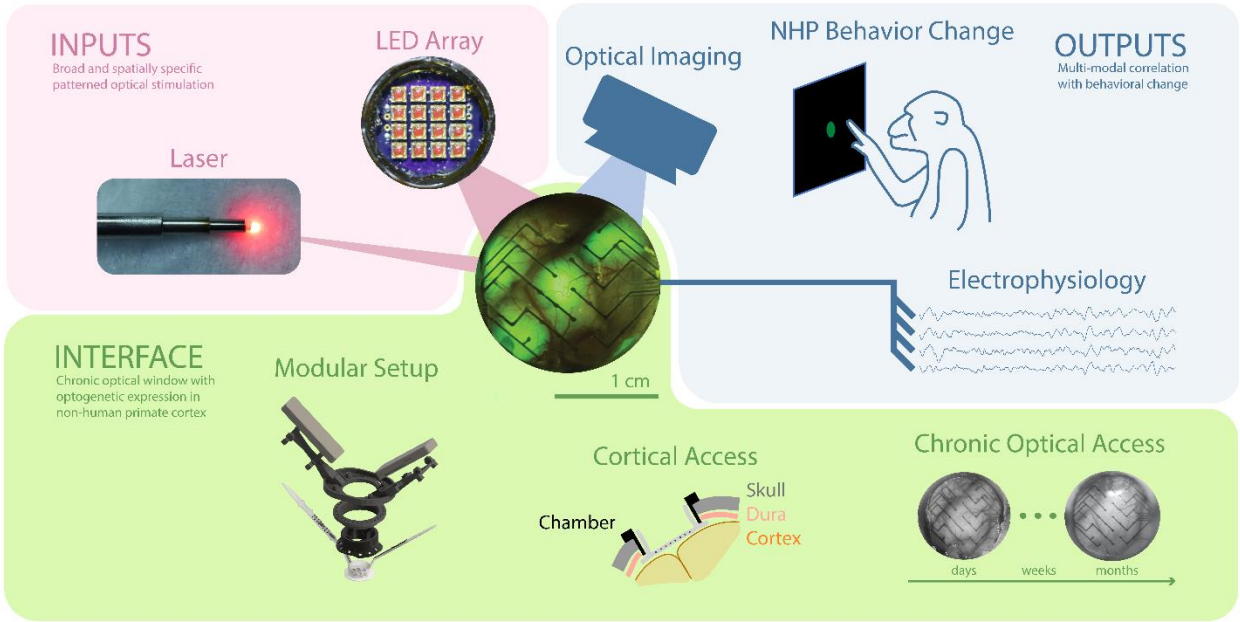

Graphical Abstract

Introduction

Optogenetics is unique among neuromodulation technologies because it allows for cell-type specific manipulation of neural networks with high spatial and temporal precision. This enables the precise manipulations needed for research in fundamental neuroscience (Carter and de Lecea, 2011; Chen *et al.*, 2013; Adhikari *et al.*, 2015; Barnett *et al.*, 2018; Camporeze *et al.*, 2018), including learning and memory (Spellman *et al.*, 2015; Barnett *et al.*, 2018; Yang *et al.*, 2018), the relationships between behavior and neural circuits in the brain (Gradinaru *et al.*, 2009; Chen *et al.*, 2013; Adhikari *et al.*, 2015; Jiang *et al.*, 2018; Yang *et al.*, 2018), the changes in neural circuitry over time (Jiang *et al.*, 2018; Yazdan-Shahmorad *et al.*, 2018), and therapies for neurological disorders (Chen *et al.*, 2013; Tønnesen, 2013; Ruggiero *et al.*, 2017; Barnett *et al.*, 2018; Camporeze *et al.*, 2018).

The evolutionary proximity between the neurophysiology of non-human primates (NHPs) and humans (Roelfsema and Treue, 2014; Lear *et al.*, 2022) spurs us to apply optogenetics to NHPs to better understand the human brain and strengthen translational medical research, especially in the context of neurological and neuropsychiatric disorders. However, studying neurological disease models in NHPs is challenging because NHP neuropathology and anomalous neural activity are often spatiotemporally complex, spanning multiple brain areas and months or years of development, much like in humans. These challenges, along with the scientific opportunities afforded by optogenetics, call for the development of large-scale, chronically-stable optogenetic platforms for NHPs. Although the development of optogenetic techniques in NHPs emerged soon after the debut of optogenetics (Han *et al.*, 2009; Diester *et al.*, 2011), its wide-spread adoption has remained a challenge. We dissect key contributing factors below that are addressed in our platform.

While optogenetics alone is a potent technique for functional neuropathological studies, the integration of optogenetics with an electrical platform, such as electrocorticography (ECoG) recordings, can enable precise optical control over specific cell types with concurrent measurement of neural activity at high spatiotemporal resolution. Merging of optogenetic and electrical platforms has been demonstrated in rodent work (Richner *et al.*, 2014; Renz *et al.*, 2020), however, similar attempts in NHP work have come with limitations. Systems where skin is closed over the implant require surgeries for device replacements or modifications and prevent ongoing assessment of both optical occlusions between the light source and the brain, as well as optogenetic expression (Komatsu *et al.*, 2017), which is typically confirmed with optical techniques. Such limitations make these systems experimentally inflexible.

In contrast, modular chambers enabling chronic access to the brain have been developed. In particular, *in vivo* optical imaging of NHP brains through cranial windows has been a small but vibrant field with decades of development (Arieli *et al.*, 2002; Slovin *et al.*, 2002; Ruiz *et al.*, 2013; A Yazdan-Shahmorad *et al.*, 2016; Yazdan-Shahmorad *et al.*, 2018; Macknik *et al.*, 2019). Optical windows to the NHP brain are often covered with a transparent, silicone-based artificial dura to protect the brain while providing optical access to the cortex (Arieli *et al.*, 2002; Slovin *et al.*, 2002; Ruiz *et al.*, 2013; A Yazdan-Shahmorad *et al.*, 2016). The artificial dura has been combined with optical stimulation methods such as infrared neural stimulation (Chernov and Roe, 2014) and optogenetics (Ruiz *et al.*, 2013; Zaraza *et al.*, 2020). In addition, we have combined electrical recording and stimulation methods using µECoG with optogenetics via an optical window. However, long-term optical access stability in these approaches remained an unmet challenge. One approach relied on daily explantation of an artificial dura and implantation of a µECoG array to perform experiments, but the frequent manipulation of the cortical surface stimulated tissue growth over the cortex and obscured optical access (A Yazdan-Shahmorad *et al.*, 2016; Devon J. Griggs *et al.*, 2021). Another approach relied on chronic co-implantation of both an artificial dura and a µECoG array between the artificial dura and the brain, but tissue growth between the artificial dura and the µECoG array obscured optical access (Yazdan-Shahmorad *et al.*, 2015; Devon J. Griggs *et al.*, 2021). To

take full advantage of optogenetics in NHPs, there is a need for innovative platforms with chronic stability in both electrophysiology and optical access to empower widespread adoption.

One obstacle in NHP optogenetics, not present in rodent models, is the size of NHP brains, which renders widespread viral delivery of optogenetic vectors impractical via traditional, diffusion-based methods. In contrast, convection-enhanced delivery (CED) is a pressure-based approach of infusion allowing for large-scale and even distribution of viral expression in comparison to diffusion-based approaches (Krauze *et al.*, 2005; A Yazdan-Shahmorad *et al.*, 2016). Previously published CED protocols relied on live magnetic resonance imaging (MRI) to monitor infusions (A Yazdan-Shahmorad *et al.*, 2016), making these methods technically challenging and only accessible to the institutions capable of MRI-guided viral infusions in NHP brain.

Given the challenges of attaining large-scale optogenetic coverage and maintaining optical access, large-scale optical stimulation techniques have been largely undeveloped – optogenetic stimulation in NHPs is generally performed by fiber optics or optrodes coupled to lasers (Tremblay *et al.*, 2020), which are not optimized for large-area optogenetic coverage. LED arrays, both with (Komatsu *et al.*, 2017) and without (Rajalingham *et al.*, 2021) simultaneous recording, have also been used, but with limited or non-contiguous cortical coverage. Optogenetic transduction and stimulation methods that are both experimentally flexible and widely accessible are necessary to capitalize on large-scale optogenetics in NHPs.

In this paper, we address the above challenges by designing accessible tools and integrating them into a single platform. We demonstrate large-scale, chronically-stable optogenetics and ECoG in an imaging window on NHP cortex. We present an optogenetic platform comprised of five complimentary state-of-the-art technological advancements, enhancing both experimental flexibility and accessibly to researchers with diverse technical backgrounds. Our advancements are: (1) a platform designed to be modular and flexible for varied, multi-modal use-cases; (2) a chronically implanted integration of an ECoG array and an artificial dura, which we refer to as a multi-modal artificial dura (MMAD); (3) optical hardware scalable from single lasers up to large arrays of LEDs for complex patterned stimulation across multiple brain areas; (4) improved ECoG-compatible optical access with the MMAD, facilitating long-term multi-modal experimentation; and (5) CED without live-MRI guidance, which is an accessible viral vector delivery method for achieving large-scale expression. These technologies are synergistic yet maintain functional modularity, i.e., no one technology requires all the others to function, thus keeping our platform relevant for experiments requiring fewer than our full suite of technologies, while maintaining forward compatibility. Our work is poised to bridge the gap between rodents and humans by facilitating powerful, multi-modal studies in NHPs.

We demonstrated the efficacy of our advancements by three complimentary measures: optical imaging, electrophysiology, and behavior. We present months of continuous optical clarity with the MMAD and years of chamber stability, which opens opportunities for translational studies of models of neurological diseases and disorders such as stroke recovery (Khanna *et al.*, 2021). The optical clarity empowered verification of large-scale epifluorescence, the product of our viral delivery process, and our ECoG recordings confirmed the flexibility of our scalable optical stimulation setup for optogenetic experimentation. We demonstrated our platform's relevance for behavioral studies by optogenetically disrupting a center-our reach task by deactivating the posterior parietal cortex (PPC). This showcases the applicability of our platform for complex behavioral experiments, and provides a milestone proof-of-concept for NHP behavior experiments with inhibitory opsins which, up to this point, have not been successfully applied to musculoskeletal movement.

The ability to link millisecond-resolution neural activity with behavioral effects and optogenetic neuronal manipulation is an invaluable addition to the NHP researcher's toolbox. Therefore, we took measures to ensure the accessibility of our methods for a diverse range of specialties: design files are provided for parts and equipment that are not commercially available, our in-house fabrication processes require only generic equipment and modest skill, and our neural processing code is publicly available. Collectively, our work enables large-scale and long-term interrogation of cortical areas in awake behaving NHPs (Griggs, 2022; Bloch, 2023).

Results

Hardware

We designed and implemented our platform for two healthy adult male rhesus macaques (*Macaca mulatta*, monkeys H and L). We used magnetic resonance imaging (MRI)-based methods to plan a craniotomy with a diameter (Ø) of 25 mm over the left PPC and to design a custom chamber with a curvature precisely fitting the surface of the skull around the craniotomy for each monkey (Fig. 1A, B). We have previously published these methods as step-by-step protocols for accessibility (Ojemann *et al.*, 2020; Iritani *et al.*, 2024). The custom chamber was designed to provide a sturdy base for experimental equipment and protect the brain when the monkey is freely moving between experiments. The chamber is further described in Methods. We implanted the chamber along with our multi-modal artificial dura (MMAD; Fig. 1C, D; (Devon J Griggs *et al.*, 2021)) in both animals. The chambers continue to be stable after 3 and >2 years following implantation for monkeys H and L, respectively.

We designed the MMAD to serve both as an optical window to the brain and as an electrocorticography (ECoG) array. The MMAD is composed of a flexible and corrosion resistant electrode array molded in silicone into a "top-hat" shape common for traditional artificial duras (Griggs *et al.*, 2019; Iritani *et al.*, 2024). The opaque, conductive traces of the MMAD are layered on top of each other to maximize the optical access to the brain through the transparent polymer of the MMAD (Devon J Griggs *et al.*, 2021). Like traditional artificial duras, the MMAD protects the brain and keeps the brain moist during experiments. Unlike traditional artificial duras, cables extend from the "top-hat" of the MMAD to hardware for electrophysiological recordings, as described below. We packaged the MMAD cables inside the chamber between experiments (Fig. 1D). The MMAD, as well as the commercially available electrode array (Ripple Neuro, Salt Lake City, UT) from which the MMAD was fabricated, are further described in Methods.

The MMAD cables require adapters, called clamp connectors, to be used with external electrophysiology equipment. We designed a stack-up of parts to attach to the chamber and support the clamp connectors (Fig. 1E, F). All parts are designed to be modular for flexible experimentation and design iterations as needed. Further descriptions of parts can be found in Methods, and design files are publicly available (find links in Methods).

Figure 1: Hardware and skull model. ***(A)*** *Digital representation of the skull with craniotomy.* ***(B)*** *Chamber custom-fit to the skull.* ***(C)*** *Molded MMAD.* ***(D)*** *Implanted chamber and MMAD packaged inside while cables are housed in the concentric grooves.* ***(E)*** *Model of electrophysiological recording hardware, top view and* ***(F)*** *trimetric view. From bottom up: MMAD, chamber, ring, clamp connector tray, clamp connectors.* ***(G)*** *LED-based optical stimulation hardware. From bottom up: Stimulation holder, cover glass, tube, LED array, rod.*

We designed and tested our platform for both laser- and LED-based optical stimulation. The lasers and optical fibers were commercially sourced and can support a variety of light wavelengths (see Methods for further laser system details). We designed an LED array and its driving circuitry in-house (Fig. 2, Supp. Fig. 1). While pulse-width modulation is a popular technique for driving LEDs, we designed our driving circuitry to be controlled by analog signals. Specifically, we drove our LEDs with continuous voltage signals to avoid high-frequency photo-induced artifacts in our electrophysiology recordings. We selected LEDs for optimal tissue penetration, and powered our circuitry with two rechargeable 9V batteries to mitigate line noise (Supp. Fig. 1). We designed and fabricated two versions of an LED array for patterned stimulation, a 4 × 4 array with individually drivable columns (Griggs *et al.*, 2022a) and a 3 × 5 array with independently drivable LEDs (Fig. 2A). Both boards used identical schematics for the driving circuitry except for the number of LEDs driven by each driving circuit (Supp. Fig. 1). We fabricated our LED arrays in two wavelengths (634 nm and 485 nm). The LED array was protected from potential moisture from the brain by a cover glass between the LED array and the MMAD (Fig. 1E-G, 2B). This also provided a small air gap between the LEDs and the cover glass to mitigate conductive heating of the brain (Fig. 2B), which is a common concern of LED-based optogenetics. We commercially sourced our custom printed circuit boards (PCBs) and assembled the LED array and driver boards in-house with common soldering methods. (For more details, see Methods.)

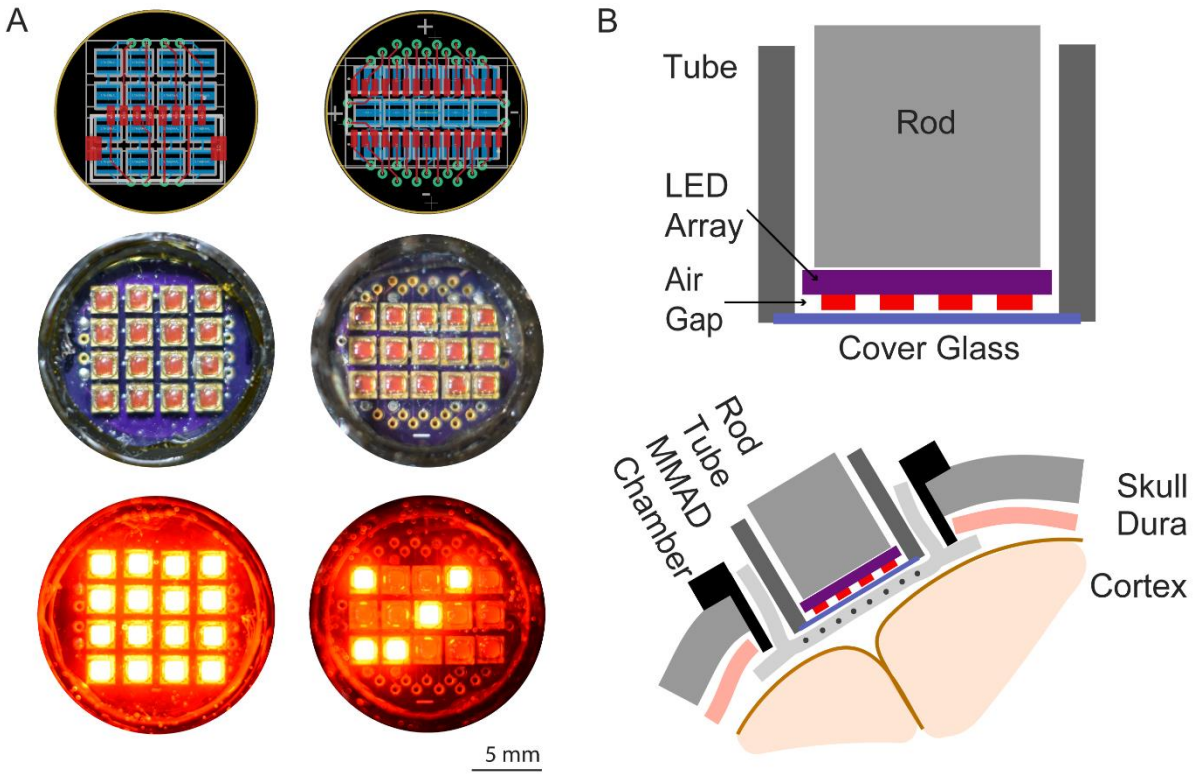

Figure 2: LED array. ***(A)*** *Row-drivable 4 × 4 LED array (left column) and individually drivable 3 × 5 LED array (right column). PCB schematic (top), photograph of LED array in tube and behind cover glass with LEDs off (middle) and on in example illumination configurations (bottom).* ***(B)*** *Schematic of LED array and related hardware for optical stimulation through MMAD, including an air gap to mitigate tissue heating.*

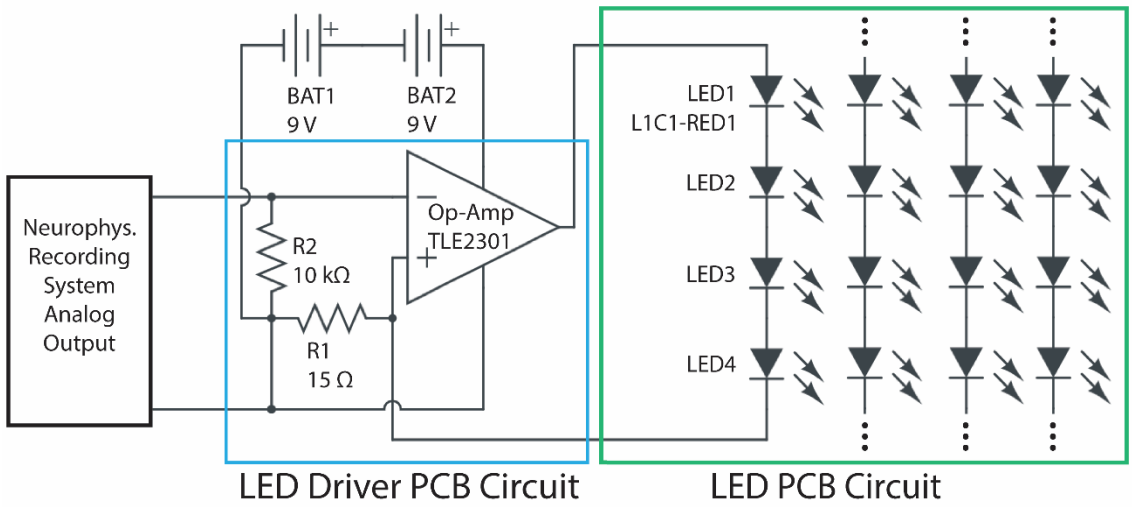

Supp. Fig. 1: Diagram of LED driving circuitry for the 4 × 4 array, which has four individually drivable rows of four LEDs each. The 3 × 5 array, which has 15 individually drivable LEDs, has identical circuitry except each LED Driver PCB Circuit drives only one LED, rather than four in series.

Optical stability

To demonstrate the stability of optical access through the MMAD we used both optical imaging and stimulation. With our MMAD, we had 10-14 contiguous weeks of optical access with both monkeys before tissue growth obscured light penetration. After tissue had matured, we resected the tissue and reimplanted the MMAD for additional experiments.

As aforementioned, both implanted monkeys have been stable for ~3 and ~2 years following surgery, and the chambers have supported optical experiments, displaying the platform's ability to facilitate long-term NHP studies. Over this period, we have repeated the dura resection and reimplantation of the MMAD for both monkeys, each allowing us windows of >10 weeks of optical access for experimentation. In addition, we confirmed the feasibility of ECoG recording using the MMAD when the dura had fully regrown underneath the MMAD (data not shown). In some instances, we observed accelerated tissue growth when we explanted the MMAD to test other recording systems. For example, following a tissue resection in monkey H approximately two years after first implantation, the MMAD was replaced and clear optical access was maintained for 7 weeks. At week 7, while optical access was still clear, the MMAD was removed to test other stimulation and recording devices that impacted tissue growth. Approximately one week later, tissue began to grow over the cortex. For another example, one and a half years after first implantation in monkey L, a similar procedure provided clear optical access for at least 5.5 weeks during which we ran experiments. Similarly, here the MMAD was removed for other experimentation that led to tissue growth. These results collectively show the stability of optical access with our design for several months and the modularity of our platform to test other recording and stimulation devices. In addition, our results caution that explantation and implantation of MMAD must be minimized, because it is known that mechanical manipulation on the surface of the brain causes irritation of the cortical surface and can lead to accelerated tissue growth that obscures optical access.

CED and epifluorescence

During the chamber implantation surgery, we used CED (similar to (A Yazdan-Shahmorad *et al.*, 2016; Yazdan-Shahmorad *et al.*, 2018; Karam Khateeb *et al.*, 2019; Griggs *et al.*, 2022b)) to infuse a pan-neuronal inhibitory optogenetic viral vector (AAV8-hSyn-Jaws-GPF) (Chuong *et al.*, 2014; Acker *et al.*, 2016) at several locations across the craniotomy. We delivered viral vector at rates up to 5 µL/min using our custom-built stepped-tip cannula (A Yazdan-Shahmorad *et al.*, 2016). Further descriptions of parts, equipment, and protocols are provided in Methods.

We infused the optogenetic viral vector in the surgery suite immediately prior to chamber implantation. This allowed us to visually inspect any potential reflux on the surface of the brain from the cannula, eliminating the need for live-MRI, which we had used in previous protocols. For this new protocol, we had eleven successful and two unsuccessful infusions as determined by epifluorecent expression near the locations of cannula insertion. We canceled one infusion before its completion because the brain did not seal against the cannula and we observed fluid buildup, likely reflux (Fig. 3B, C). We reattempted that infusion nearby, and successfully generated expression (Fig. 3B). In the first surgery (monkey H), we had difficulty determining the depth of cannula penetration into the brain with stereotactic instruments alone because of the brain's tendency to dimple during cannula insertion. To address this in our second surgery (monkey L), we marked the cannula prior to surgery at a set length distal from the cannula's tip to facilitate measurement of penetration depth during surgery. This technique correlated with an

improvement in success rate between our first and second surgeries (62% and 100%, respectively; Fig. 3B).

Our long-term and large-scale optical access provided by the MMAD empowered us to monitor optogenetic expression over time for both monkeys. Monkey H underwent initial imaging for epifluorescence two weeks after viral infusion. Expression was evident during the first imaging session and increased in coverage and intensity until the fifth week after infusion, when expression plateaued at 92 mm^2 coverage (Fig. 3A-B). Similarly, we confirmed 76 mm^2 expression coverage in monkey L (Fig. 3B). Although we did not see a change in epifluorescent expression during the initial months following viral injection, approximately two years after infusion we observed a significant reduction of expression in both monkeys (data not shown).

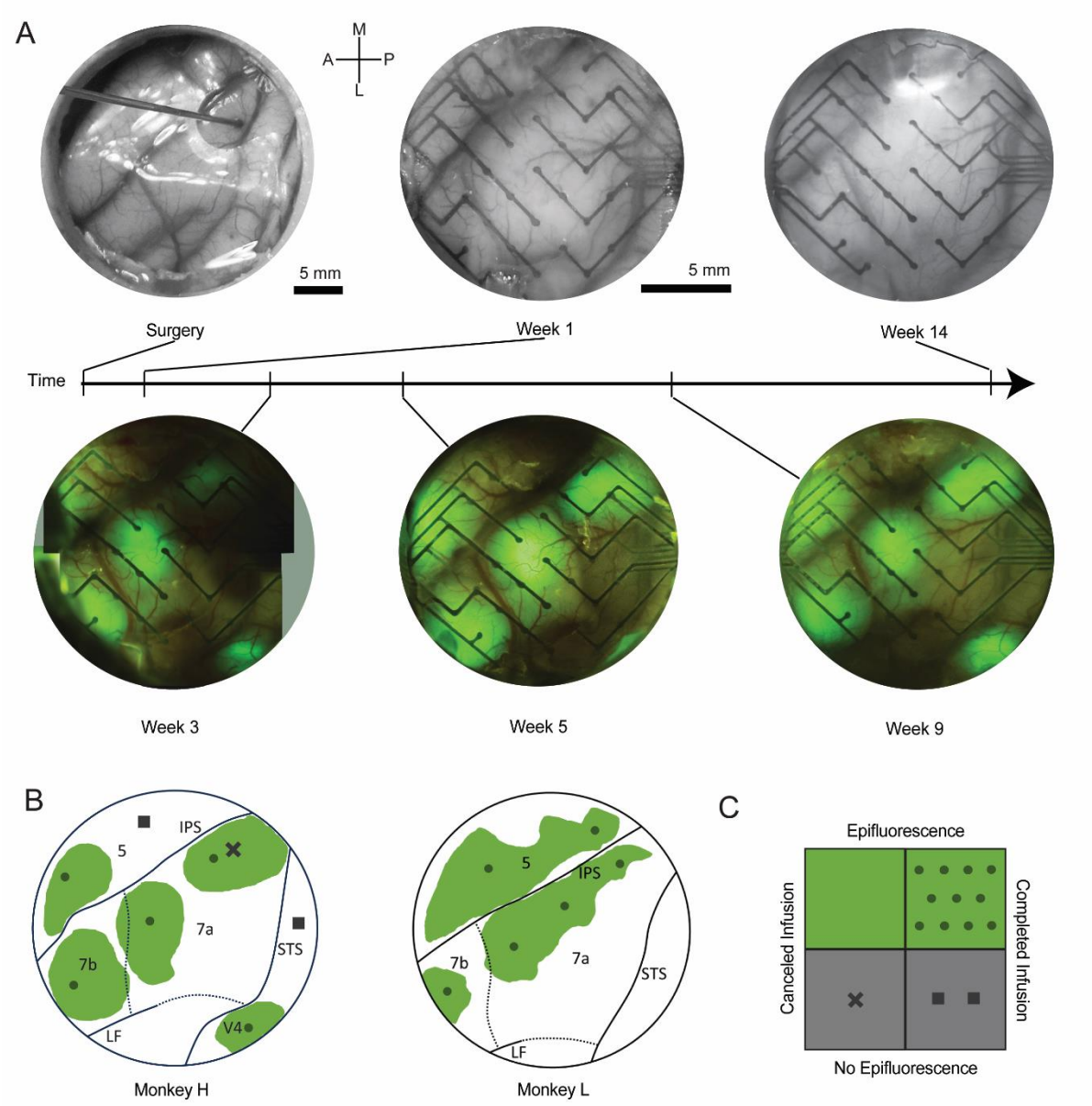

Figure 3: Optical window and epifluorescence. ***(A)*** *Optical access (top) and epifluorescence (bottom) for monkey H over time. CED was performed through a hole in a temporary artificial dura during surgery to virally transfect tissue (top left).* ***(B)*** *Expression maps based on epifluorescence (green) for monkeys H (left, first monkey to undergo surgery) and L (right, second monkey to undergo surgery). Approximate locations of successful (green dots) and unsuccessful (grey squares) CED infusions. One infusion was canceled before completion (grey ×) and a second infusion attempt was made nearby, which was successful.* ***(C)*** *Summary of CED infusions across both monkeys.*

Stimulation at rest

To demonstrate our platform's ability to integrate optogenetics and ECoG, we applied various optical stimulation protocols (Fig. 4A, F, K) and recorded evoked neural activity. We removed photo-induced artifact as described in Methods. Statistical tests were run by comparing the neural activity to the baseline recording before the onset of stimulation.

Stimulation with all 16 red (634 nm) LEDs of the 4 × 4 array during rest in monkey L produced a significant increase in ECoG power (Fig. 6A-C), which was contrary to our expectations for an inhibitory opsin. We then proceeded to validate that our light-evoked responses were optogenetically induced by designing multiple control experiments. For the first control experiment, we repeated our standard red stimulation after tissue growth between the brain and the MMAD had completely obscured optical access (Fig. 4A). We predicted that the tissue growth would reduce the optical power reaching the brain and thus reduce the evoked response in comparison to stimulation with clear optical access. This was confirmed in the data but not to a statistically significant degree (Fig. 4B, D). For the second control experiment, we selected an off-peak wavelength (blue, 485 nm), which is more absorbed by the brain tissue than our standard red wavelength, to sub-optimally drive the Jaws opsin through a clear optical window and test the impact of heat (Fig. 4A). We observed increased ECoG power with the control wavelength (Fig. 4B, E), but to a significantly lesser extent than our standard wavelength (Fig. 4B, C). This suggests ECoG responses are primarily optogenetically-evoked, and not thermally-evoked.

We also investigated the local inhibition of the network using our modular LED array as well as lasers. To test our modular 3 × 5 LED array, we illuminated a small region of Monkey L's brain with only a single red LED (Fig. 4F). Evoked activity was observed on the channels first (Fig. 4G, H) and second (Fig. 4G, I) most proximal to the illuminated brain region. All other channels did not show stimulation-induced modulation (Fig. 4G, J). Results display our LED array's capability of stimulating in spatiotemporally precise patterns.

To demonstrate the versatility of our platform, and specifically it's compatibility with lasers, we illuminated neural tissue of monkey H with fiberoptic cable near selected electrodes and evoked spatially specific changes in our neural recording (Fig. 4K). Results are shown at the site of stimulation (Fig. 4L, M) and at untargeted sites (Fig. 4L, N, O). Unlike the activation profile from the single LED illumination, the laser-evoked activity was only visible on a single channel, demonstrating tighter spatial localization, as expected.

Next, we assess the spatial nature of the neural responses with respect to opsin expressing and opsin deficient areas. To do so, we stimulated all 16 red LEDs of the 4 × 4 array during rest and separated recording channels based on the expression in their vicinity. For both monkeys, ECoG power evoked by red LEDs was stronger in the expressing areas than the opsin deficient areas (Monkey H: $p = 0.0115$; Monkey L: $p = 9.056e-22$) (Fig 5). These data contrast with the results of sub-optimal stimulation techniques, being red LED stimulation with tissue growth over the brain and blue LED stimulation of a clear window, where there was no significance between the opsin expressing and opsin deficient areas (Fig 5D). When comparing evoked responses during rest and behavior, we found that red LED stimulation of a clear optical window produced greater ECoG responses in opsin expressing areas than in opsin deficient areas for both conditions, while no difference was observed during behavior without stimulation (Supp. Fig. 2; behavior described below). These results further support our finding that

optical stimulation of neural tissue expressing Jaws increased ECoG power, despite Jaws being an inhibitory opsin.

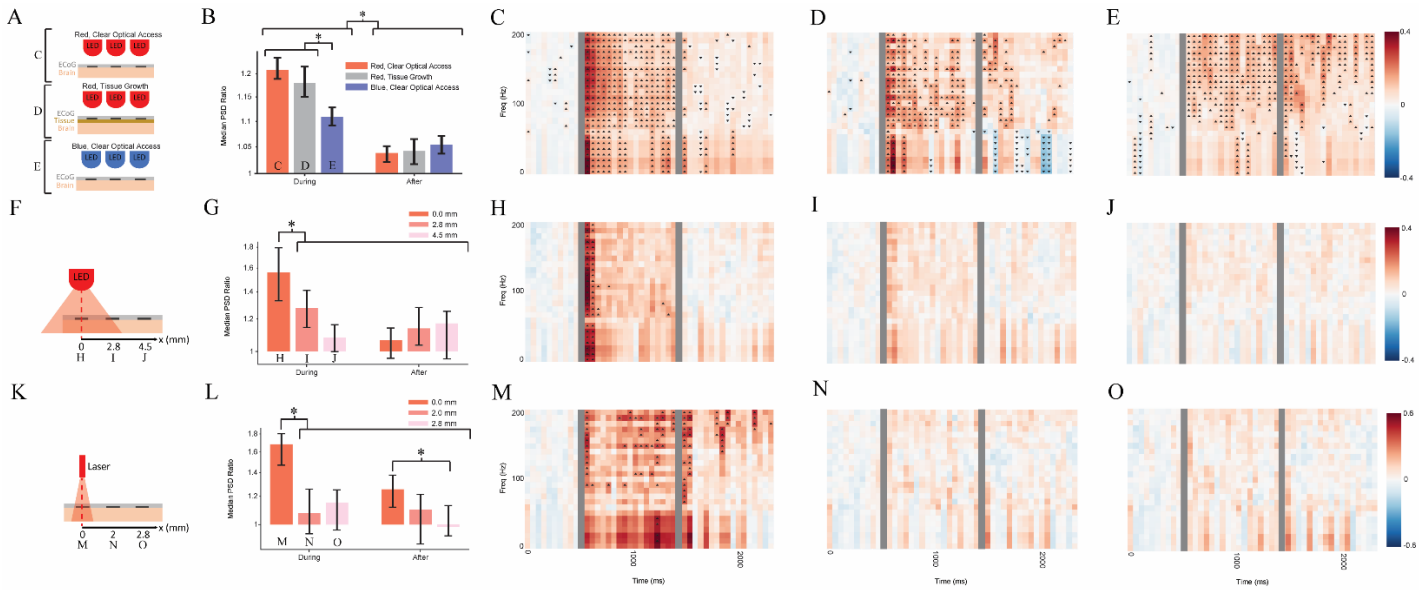

Figure 4: Neural response to stimulation protocols when the monkey was at rest. ***(A, F, K)*** *Schematics of optical stimulation protocols. (A): full 4 × 4 red LED array with clear optical access (C), full 4 × 4 red LED array with tissue growth between the MMAD and brain (D), full 4 × 4 blue LED array with clear optical access (E). (F): single red LED at varying distances from the recording electrode (H-J). (K): single red laser at varying distances from the recording electrode (M-O).* ***(B, G, L)*** *Median of the broadband power ratio for both during and after stimulation, as compared with before stimulation, for different stimulation protocols. Whiskers are 95% confidence intervals of the medians, and asterisks indicate significant differences between the conditions (Bonferroni correction applied to $p < 0.05$). The callouts at the base of the bars indicates the subpanel represented in that specific bar of the bar chart.* ***(C-E, H-J, M-O)*** *Spectrograms are average neural activity across trials for the 900 ms stimulation and the 500 ms before the onset of the stimulation and 900 ms after the offset of stimulation. Grey bars indicate bins during the first 50 ms of stimulation onset and offset – data during these times are excluded due to residual artifact after artifact removal. Full LED array stimulation was averaged over all channels and performed in three conditions: red light with clear optical access (C), red light with tissue growth obscuring the brain (D), and blue light with clear optical access (E). Single red LED stimulation was performed with three conditions: illumination directly over, 2.8 mm from, and 4.5 mm from the recording channel (H, I, J, respectively). Single red laser stimulation was performed with three conditions: illumination directly over, 2.0 mm from, and 2.8 mm from the recording channel (M, N, O, respectively). Spectrograms normalized by frequency with the 500 ms recording immediately prior to stimulation, and the log base 10 of the values are shown. Arrowheads indicate significant ($p < 0.05$) differences between the conditions, and direction of significance.*

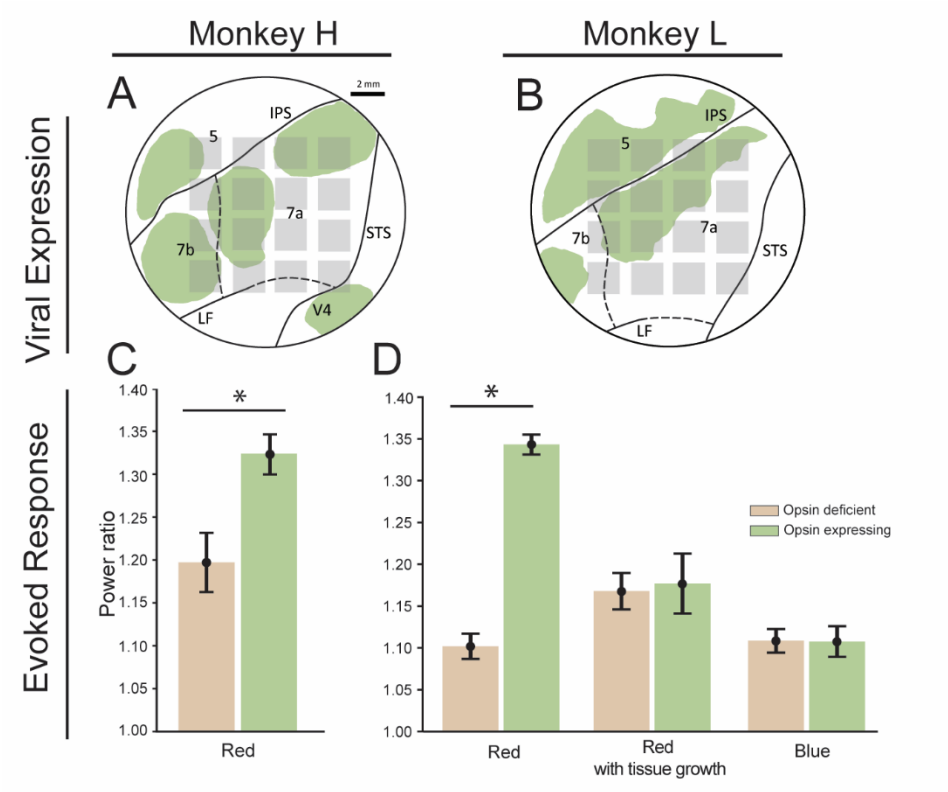

Figure 5: Map of neural responses with respect to opsin expressing and opsin deficient areas. ***(A, B)*** *Epifluorescent maps and approximate LED locations for monkeys H and L, respectively.* ***(C, D)*** *Median evoked responses in opsin deficient and expressing areas for monkeys H (C) and L (D). For monkey L, evoked responses are also shown under control stimulation conditions of red light with tissue growth and blue light with clear optical access (depicted in Fig. 4A). The power ratios of responses are calculated between the ECoG recordings from during verses before stimulation. Whiskers are standard error of the mean. Asterisks indicate significant differences between conditions ($p < 0.05$, Mann-Whitney U-test).*

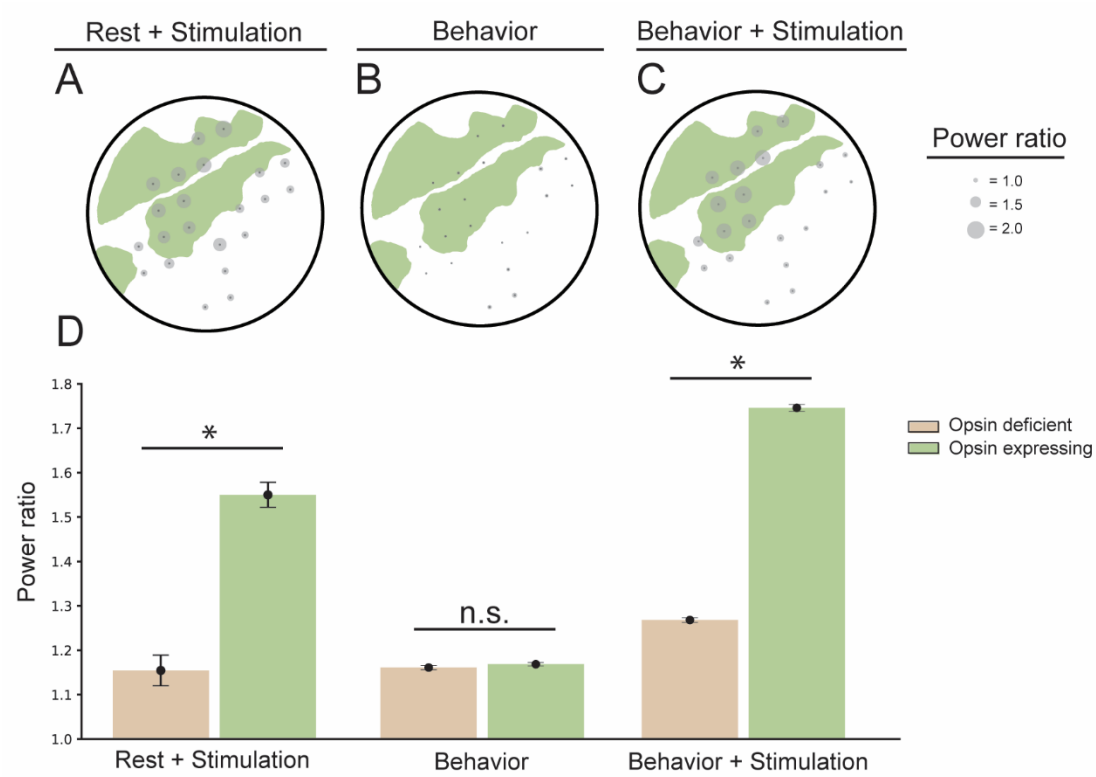

Supp. Fig. 2: Maps of neural responses with respect to opsin expressing and opsin deficient areas and with respect to behavioral state. ***(A-C)*** *Epifluorescent maps and approximate electrode locations for monkey L.* ***(D)*** *Median evoked responses in opsin deficient and expressing areas under different stimulation conditions (i.e., stimulation with red LEDs or no stimulation) and different behavioral conditions (i.e., performing a reach behavior or at rest). The power ratios of responses are calculated between the ECoG recordings from during versus before stimulation. Whiskers are standard error of the mean. Asterisks indicate significant differences between conditions ($p < 0.05$, Mann-Whitney U-test).*

Stimulation during behavior

To demonstrate our platform's applicability for behavioral neuroscience experiments, we trained the monkeys to perform a center-out reach task using their right hand (contralateral to the implant, Fig. 6A). The monkey held his finger at a start target in the center of a screen, and then the end target displayed on the screen randomly in four locations: right, up, left, and down. We applied optical stimulation for 900 ms with all LEDs of our red 4 × 4 array (~12 mW/mm^2) simultaneously for a randomly selected 50% of the trials with the expectation that optogenetic inhibition would slow reach. The onset of the stimulation aligned with the appearance of the end target. After a random delay, an audial "go-tone" would play, signaling the monkey to reach for the end target. Monkeys typically completed the reach within 900 ms of the end target being displayed.

We tracked the reach path between the go-tone and the finger's entry into the end target, and analyzed movement in three-dimensional space (two dimensions shown in Fig. 6B-C) for both stimulation and control (no stimulation) conditions. We measured the time between the go-tone and the finger's entry into the end target, and we call this time length the "total time." The total time is the sum of two parts, being the time taken for the monkey's finger to exit the start target, which we call the "reaction time," and the time taken to complete the reach from that point, which we call the "movement time." We

found that optogenetic inhibition resulted in significantly longer reaction times and total times for both monkeys. In one monkey, movement time was also significantly longer.

For monkey H, leftward and rightward reaches under stimulation had significantly longer reaction times and total times (reaction time left: p = 0.02877; right: p = 0.00856; total time left: p = 0.002255; right: p = 0.02668) (Fig. 6F). Rightward reaches under stimulation had significantly longer movement times (p = 0.000419) (Fig. 6F). When data for all four reach directions were aggregated, reaches under stimulation had significantly longer reaction times and total times (reaction: p = 0.04006; total: p = 0.02468) (Fig. 6F). For monkey L, downward and leftward reaches under stimulation had significantly longer movement times and total times (movement down: p = 1.480e-6; left: p = 0.005348; total down: p = 5.987e-6; left: p = 0.0263) (Fig. 6G). Upward reaches had significantly longer reaction times (p = 5.9638e-5) (Fig. 6G). When data for all four reach directions were aggregated, reaches under stimulation had significantly longer reaction times, movement times, and total times (reaction: p = .0009992; movement: p = 0.0002913; total: p = 0.0001560) (Fig. 6G).

Along with the time of each reach, we also measured path length. For monkey H, the distance traveled in the *z*-dimension (i.e., perpendicular to the screen) during stimulation is significantly greater for the leftward and rightward reaches (left: p = 0.00239; right: p = 0.0309) (Fig. 6D), which correlates with reaction time and total time significance (Fig. 6F). In contrast, the distance traveled in the *y*-dimension (i.e., up or down the screen) during stimulation was significantly lesser for the upward reaches (p = 0.0183) (Fig. 6D). When data for all four reach directions were aggregated, no statistical significance was found (Fig. 6D). For monkey L, the distance traveled in the *z*-dimension during stimulation is significantly greater for the downward and leftward reaches (down: p = 1.426e-10; left: p = 2.70e-5) (Fig. 6E), which correlates with the movement time and total time significance (Fig. 6G). The distance traveled in the *y*-dimension during stimulation is also significantly greater for the downward and leftward reaches (down: p = 9.133e-6; left: p = 0.0006849) (Fig. 6E), while the distance traveled in the *x*-dimension during stimulation was significantly greater for upward reaches (p = 0.01820) (Fig. 6E). When data for all four reach directions were aggregated, distance traveled during stimulation was significantly greater for the *y*- and *z*-dimensions (y: p = 0.00850; z: p = 1.858e-8) (Fig. 6E). Collectively, the results agree with our original hypothesis that optogenetic stimulation would slow reach.

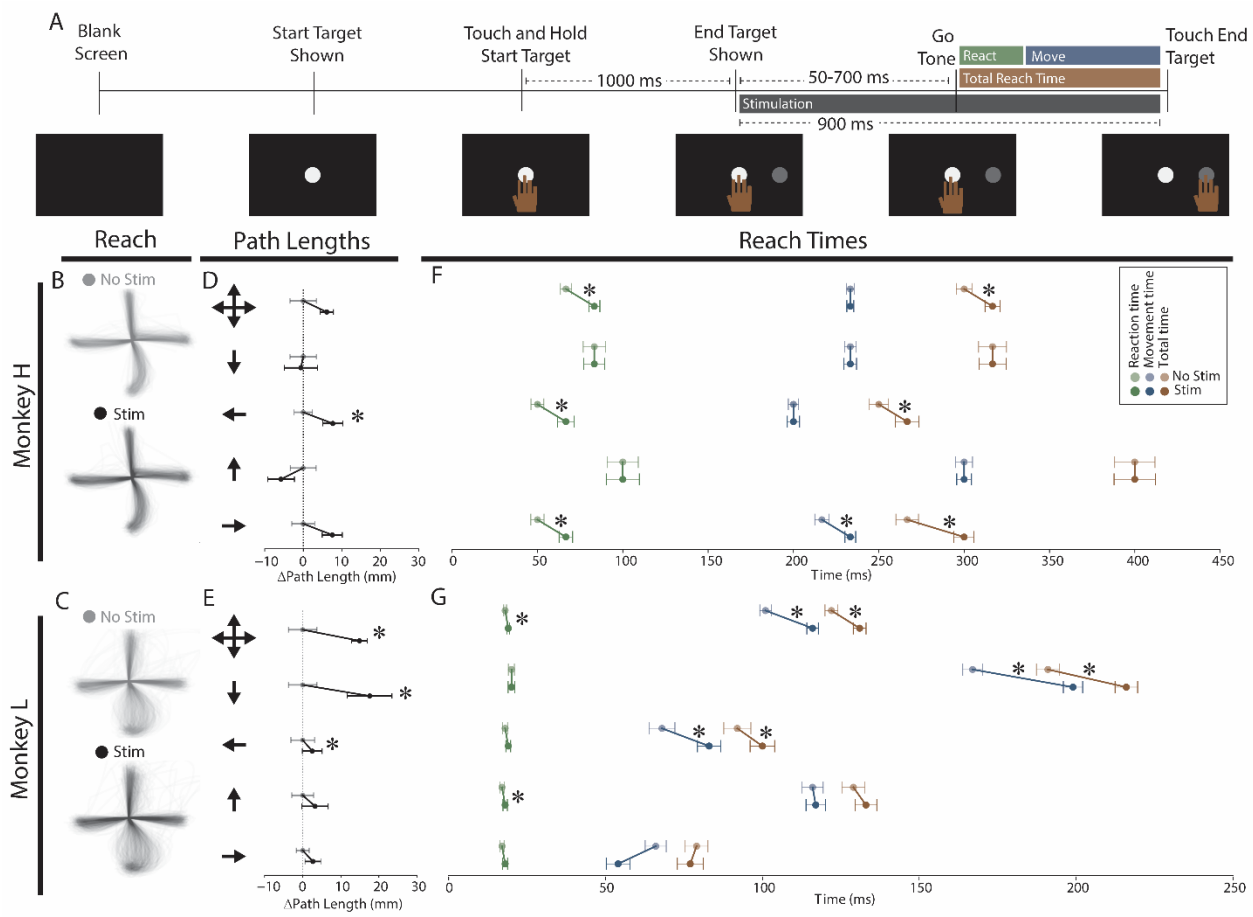

Figure 6: Behavioral task and results. ***(A)*** *Schematic of behavioral task and stimulation timeline.* ***(B, C)*** *Reach paths* ***(D, E)*** *Reach path lengths, displayed as a difference from the median path length of the control reaches.* ***(F, G)*** *Reach time medians for reaction time, movement time, and their sum, being the total time. Data are paired as a faintly colored upper point for the control condition without stimulation, and a stronger colored lower point for the stimulation condition. Reach directions for each row of data are indicated with arrows and apply to (D-G), where all four arrows together (top row of D and E) represent the aggregation of reaches in all directions. Whiskers are standard error of the mean. Asterisks denote* $p < 0.05$ *using a Mann-Whitney U-test.*

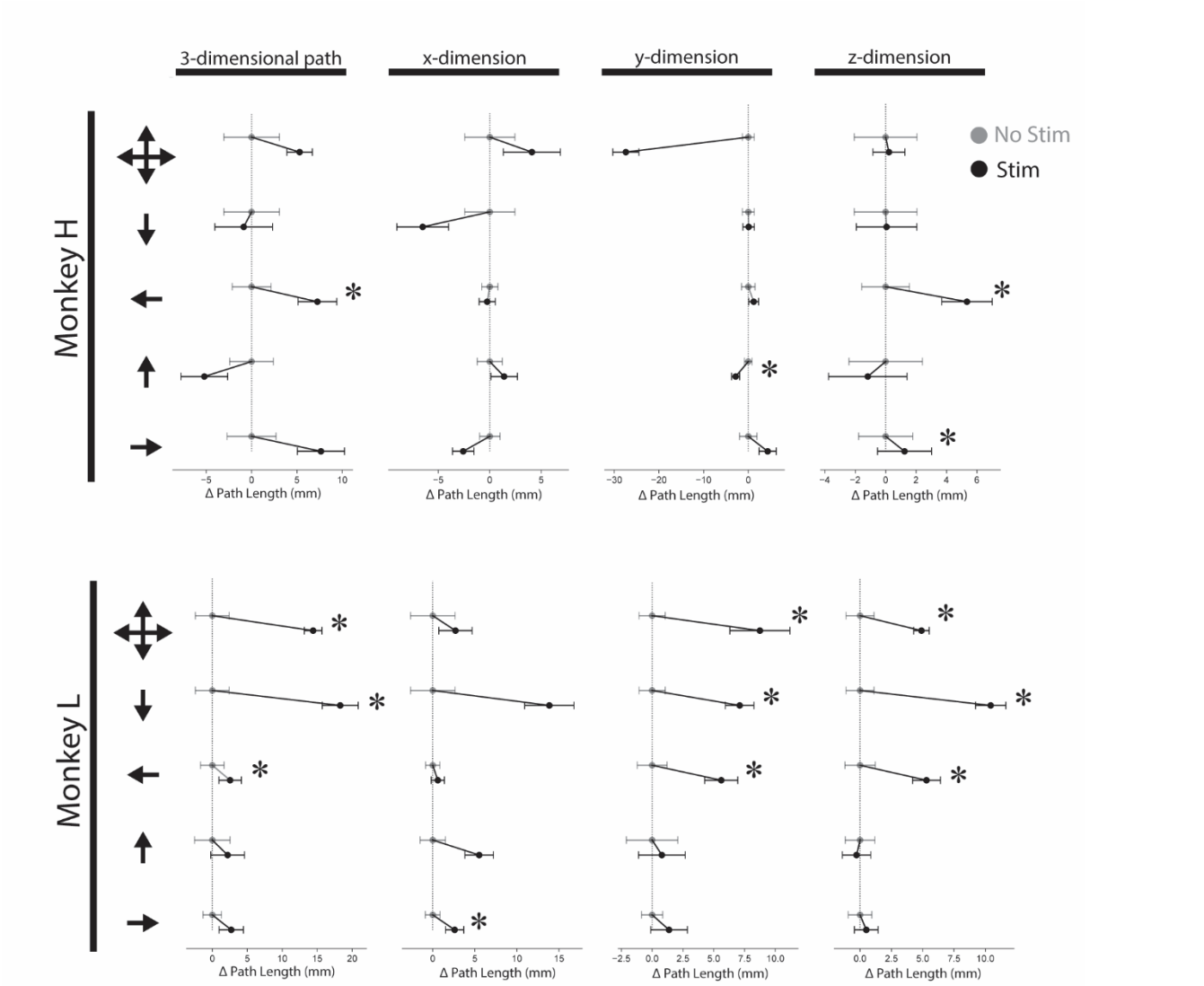

Supp. Fig. 3: Path length of finger travel from the start target to the end target during the task, displayed as a difference from the median path length of the control reaches (i.e., reaches without stimulation). Rows are path lengths for each individual reach direction, as well as all directions combined. Columns are path lengths as broken into x- (left/right across the screen), y- (up/down the screen), and z-components (away/toward the screen), as well as all three dimensions combined. Error bars are standard error of the mean. Asterisks denote $p < 0.05$ using a Mann-Whitney U-test.

We analyzed the neural activity recorded during reaches with and without optogenetic stimulation to identify the change in neural activity underlying the reach disruption (see Methods for details on the neural data analysis). During stimulation, we observe increased power throughout the time course and over most frequencies. The data show that stimulation during reach increases the brain activity over the entire course of stimulation, with nearly all time and frequency bins exhibiting significant (Bonferroni correction applied to $p < 0.05$) modulation from stimulation. The average wideband power ratio for both during and after stimulation illustrate that stimulation produces significant (Bonferroni correction applied to $p < 0.05$) electrophysiological effects for both monkeys (Fig. 7D, H). Effects are similar between monkeys, and the results are in agreement with the results of stimulation during rest (Fig. 4, Supp. Fig. 2).

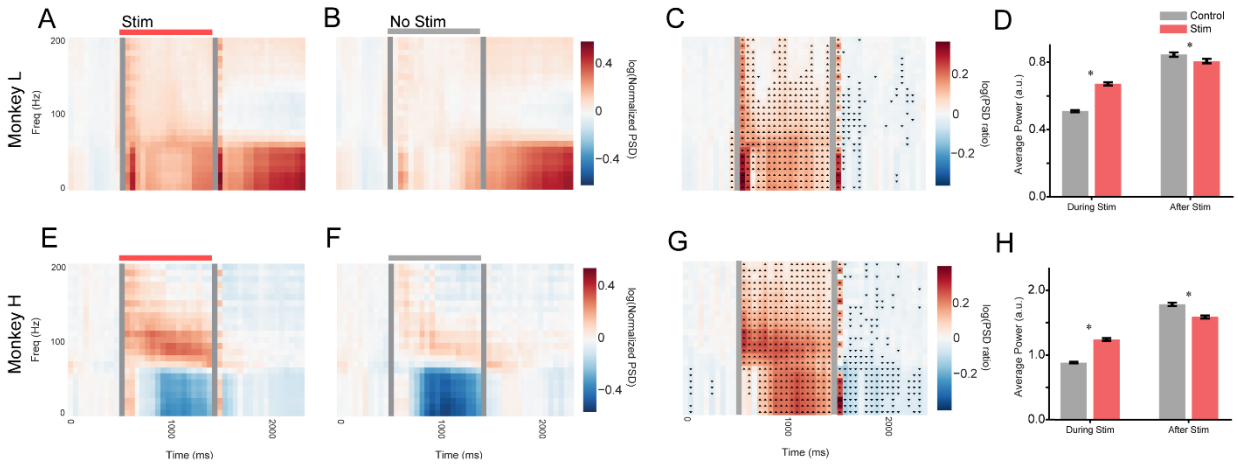

Figure 7: The effect of stimulation on neural activity during reach. ***(A-B)*** *Spectrograms of monkey L neural activity during reach in the stimulated condition (A) and in the control condition (B). Values are averaged over all trials, sessions, and channels. In the stimulated condition, the spectrogram is an average of neural activity across trials for the 900 ms stimulation of the full 4 × 4 red LED array and the 500 ms before the onset of the stimulation and 900 ms after the offset of stimulation. Grey bars indicate bins during the first 50 ms of stimulation onset and offset – data during these times are excluded due to residual artifact after artifact removal. The spectrogram is normalized by frequency with the 500 ms recording immediately prior to stimulation, and the log base 10 of the values are shown. The data processing of the control condition matches the stimulated condition, although the stimulation did not occur.* ***(C)*** *Ratio of average signal power between the stimulated (A) and control (B) neural activity during reach. Arrowheads indicate significant differences between the conditions (Bonferroni correction applied to $p < 0.05$), with the direction of the arrowhead indicating the direction of significance.* ***(D)*** *Bar chart summary of (A, B). Average power for the stimulated and control neural activity during reaching. Whiskers are 95% confidence intervals of the average, and asterisks indicate significant differences between the conditions (Bonferroni correction applied to $p < 0.05$).* ***(E-H)*** *Same as (A-D) but for monkey H.*

Discussion

We present an NHP optogenetic ECoG platform both accessible to researchers with diverse expertise and flexible for diverse experimental aims. Our work entails five complimentary technological advancements tied together with the common thread of experimental flexibility and researcher accessibly: an adaptable and modular platform, a chronic MMAD, scalable optical hardware for patterned stimulation, improved ECoG-compatible optical access, and efficient viral vector delivery without live-MRI monitoring. We demonstrated the efficacy of these advancements by three complimentary measures: optical imaging, electrophysiology, and behavior.

Platform hardware

We designed our platform to be widely accessible by making it modular and replicable in a number of ways. All parts are interchangeable between monkeys except those chronically implanted. Our MMAD molding process did not require any special facilities or tools aside from the custom mold pieces, and the miniature ECoG array is commercially available (Ripple Neuro Inc.). We have previously demonstrated the MMAD's capability of electrical stimulation (Devon J Griggs *et al.*, 2021; Khateeb *et al.*, 2022; Zhou *et al.*, 2022, 2023; Schwock *et al.*, 2024), which opens further experimental opportunities, especially given that optogenetic and electrical stimulation have been shown to work synergistically (Ohayon *et al.*, 2013; Hart *et al.*, 2020). Furthermore, we predict our work will spur the development of MMADs with higher channel counts of smaller and transparent electrodes to increase electrophysiological resolution and optical

access (Belloir *et al.*, 2022; Vargo *et al.*, 2023). We also expect LEDs will be incorporated into future MMAD designs, much like past work with electrodes arrays (e.g., (Ji *et al.*, 2018; Reddy *et al.*, 2019)). Our platform can facilitate iterative development in MMAD design because explantation of past designs and re-implantation of future designs is minimally invasive. Replacing or updating electrophysiological or optical stimulation hardware implanted with traditional window-less approaches, like Utah arrays or LED arrays sutured to the native dura (Rajalingham *et al.*, 2021), is much more challenging in comparison to our window-based method.

The ring and clamp connector tray facilitate experimental flexibility for imaging, electrophysiological recording, and both fiberoptic- and LED-based optical stimulation. Most of the optical stimulation components can be 3D printed in-house with common 3D printers, which facilitates quick and inexpensive revisions for experimental needs. Parts can be soldered onto the LED-related PCBs in-house with minimal experience, and simple, custom-designed battery-powered circuitry mitigates line-noise. The LEDs are commercially available in many colors. Our custom circuitry does not use pulse-width modulation, but drives the LEDs continuously. Continuous stimulation minimizes the count of optical stimulation onsets and offsets per stimulus, thus mitigating complexity of photo-induced artifacts in electrophysiology data. Regardless, the remaining singular onset and offset of continuous stimulation produced artifacts in our ECoG data. We rejected the artifacts with a rigorous procedure, which can be readily adapted for other experiments combining optogenetics with electrophysiology. We incorporated an air gap into our LED setup to mitigate tissue heating, which is a significant concern in all optogenetic experiments, and particularly when placing LEDs on (Rajalingham *et al.*, 2021) or in the brain. To further protect the brain from heating, we designed the LED array and the driving circuitry to be separate PCBs to keep heat produced by the driving circuitry (i.e., opamps and resisters) away from the brain. The stimulation setup of previous work allowed for the optical stimulation of only two or three point-locations at a time due to the physical interference of fiberoptic wires within the chamber (Azadeh Yazdan-Shahmorad *et al.*, 2016); in contrast, our LED array provides large-scale patterned optical stimulation for targeting several brain areas simultaneously. We anticipate development of higher-count and multicolor LED arrays to further complement our large-scale optical platform, which would be especially powerful with multi-opsin and step-function opsin experiments (Diester *et al.*, 2011). The design files of our electronic and hardware parts are publicly available (URLs in Methods).

MMAD optical access

Our work pushes the bounds of previous efforts across the field largely hindered by the challenge of maintaining optical access and especially at the large scales that will be necessary to study complex network interactions across multiple brain regions in behaving NHPs. As with past work, we resected both the skull and the opaque native dura and implanted transparent artificial duras that are biocompatible and can provide optical access to the brain for 3-9 months (Arieli *et al.*, 2002; Chen *et al.*, 2002; Azadeh Yazdan-Shahmorad *et al.*, 2016) before tissue growth stifles optical access (Azadeh Yazdan-Shahmorad *et al.*, 2016). This tissue is a neo-membrane and cannot be easily removed during early stages of growth because it is nourished through the brain, but the tissue can be surgically removed once the neo-membrane matures and separates from the brain. This growth process forces the researchers to wait for about one to two months before resuming experimentation, and thus highlights the importance of maintaining optical windows for an order of months, as others have done with classic optical windows and as we have now demonstrated with an electrocorticographic optical window.

Early works attempting to integrate electrode arrays and large-scale optical windows did not result in long-term optical access (Yazdan-Shahmorad *et al.*, 2015; A Yazdan-Shahmorad *et al.*, 2016). In this work, we achieve over 3 months of optical and electrophysiological access by embedding electrodes into a

transparent polymer (Devon J Griggs *et al.*, 2021) and then integrating the array into an artificial dura to create a single MMAD. The brain's response is similar to classic, electrode-free silicone artificial duras. While others have also embedded miniature ECoG arrays into artificial duras (Chiang *et al.*, 2020), the ECoG design restricted optical access. We integrate our MMAD, purposefully designed for optical access (Devon J Griggs *et al.*, 2021), with an artificial dura to support chronic optogenetics, imaging, and ECoG.

While others have proposed window-less designs for LED-based NHP optogenetics (Komatsu *et al.*, 2017; Rajalingham *et al.*, 2021), our work facilitates routine epifluorescent monitoring of large-scale optogenetic expression, revealing experimental insights otherwise challenging to ascertain. For example, in our experiment the optical window empowered us to confirm that CED performed without the complexity of live-MRI (unlike (A Yazdan-Shahmorad *et al.*, 2016)) resulted in a progression of large-scale expression up to a plateau in expression at 5 weeks. The large areas of epifluorescent coverage are comparable with previous work (A Yazdan-Shahmorad *et al.*, 2016). Around 2 years later we observed a waning of epifluorescent expression, which again highlights the value of window-based designs for routine optical monitoring of the cortex. Our platform also supports non-genetic optical techniques, such as infrared neural stimulation (Chernov and Roe, 2014) and photochemical lesioning (Yao and Yazdan-Shahmorad, 2018; K Khateeb *et al.*, 2019; Devon J. Griggs *et al.*, 2021; Khateeb *et al.*, 2022; Zhou *et al.*, 2022), which sets the stage for such studies to be complimented with chronic ECoG data via our MMAD. Further, our platform enables routine monitoring of tissue growth, which can be problematic for many optical techniques and is difficult to assess without an optical window.

Accessible CED protocol

Our CED success is an important proof of concept for our method of optogenetic CED in monkey cortex without live-MRI guidance. While live-MRI is a powerful method of visualizing infusions in real-time during surgery (A Yazdan-Shahmorad *et al.*, 2016; Karam Khateeb *et al.*, 2019), the method is logistically challenging or infeasible at many institutions, limiting its use. Our MRI-free CED method was performed entirely in the surgery suite and during the same surgery where all other surgical operations were performed. This eliminated the need for MRI-compatible syringe pumps and complicated fluid line setups, and instead used a setup which may be widely accommodated by surgery suites at other institutions, while still capitalizing on the efficiency of CED over traditional diffusion-based approaches.

Optogenetic effects on neurophysiology

We hypothesized that our inhibitory opsin would reduce ECoG signal power when stimulated, but we were surprised to find a general increase in ECoG signal power (Fig. 4, 5, 7), including when channels were grouped by the presence or deficiency of expression in their vicinity (Fig. 5). We suspect upper layers of the cortex, which are known to have higher ratios of inhibitory neurons than other layers (Meyer *et al.*, 2011; Kooijmans *et al.*, 2020), were more strongly inhibited due to greater proximity to the light source, thus netting higher electrophysiological signal power from lower cortical layers. In addition, we recognize the local field potentials (LFPs) we were recording represented an aggregation of neural activity, adding complexity to the interpretation of the result. Our results emphasize the field's incomplete understanding of neural activity at the network level, and therefore caution must be taken when generalizing single-cell analyses (e.g., (Chuong *et al.*, 2014)) to the network level. Specifically, our inhibition length of 900 ms is uncommonly long, the opsin kinetics of inhibition at this time length are not well studied, and simultaneous optogenetic stimulation of tens of mm^2 of cortex is underexplored. This opens the door to exploring prolonged and large-scale optogenetic stimulation protocols, especially with inhibitory optogenetics, given that such protocols are not likely to be well-approximated by electrical

stimulation methods. Although increase in signal power during optogenetic stimulation was unexpected, our control experiments validated that the increase in signal power was, indeed, optogenetically evoked (Fig. 4). Lasers generated more spatially specific modulation than LEDs, and red light provided stronger neural modulation than blue light in accordance with the spectral characteristics of Jaws (Chuong *et al.*, 2014; Acker *et al.*, 2016). The latter observation would not be expected had neural responses been merely an effect of tissue heating as blue light is absorbed more than red light and thus causes more spatially specific heating (Jacques, 2013). As a further control, when the channels were grouped by the presence or deficiency of expression in their vicinity, red stimulation through tissue growth and blue stimulation with clear optical access experiments failed to generate statistically significant results, leaving red stimulation with clear optical access as the only case where opsin expressing areas were evoked to higher power than opsin deficient areas (Fig. 5).

Optogenetic effects on behavior

In this work, we disrupted sensory-guided reaching behavior using an inhibitory opsin. Past studies have attempted to use excitatory opsins to evoke musculoskeletal activity in NHPs at rest; early trials were unsuccessful (Diester *et al.*, 2011), but more recently, a proof-of-concept was demonstrated (Watanabe *et al.*, 2020). Building on this work, a preprint study has disrupted sensory-guided reaching behavior using excitatory optogenetics (O'Shea *et al.*, 2022). However, to our knowledge, this is the first report of reach disruption using an inhibitory opsin in NHPs, which opens a new class of experiments to the field.

We used a center-out reach task to test for optogenetic behavioral modulation, and we disrupted reaches in two monkeys, as confirmed with both spatial and temporal metrics. Specifically, we confirmed our hypothesis that inhibition of the PPC, a sensory integration area of the brain, would slow reaches informed by audial and visual cues. The direction-specific variation of behavioral modulation between monkeys is likely due mostly to the variance in opsin expression maps (Fig. 3B). Differences in signal power between stimulation during reaches and at rest (Figs. 7A, 4G) indicate that the behavioral context affects the spatiotemporal frequency characteristics of stimulated neural systems (Bloch *et al.*, 2022). Of note, reaches were qualitatively similar with and without stimulation (Fig. 6A), demonstrating that optogenetics can modulate reach while largely preserving natural and voluntary characteristics of the reach. However, our observation that stimulation altered reach path characteristics to statistically significant degrees (Fig. 6A) suggests further need for studies on the motor dynamics of reach. Our results indicate that our platform is suitable for studying neural mechanisms of behavior with millisecond-precision, spatial specificity, and reversable modulation of a variety of brain areas.

Collectively, our methods make cutting-edge neuroengineering techniques approachable to NHP researchers with diverse expertise. Our results validate our chronic setup and indicate its suitability for large-scale and long-term stimulation and recording experiments in behaving monkeys. The combination of high temporal and spatial precision with large-scale and long-term access renders our platform particularly useful for experiments which need fine-scale manipulation and sensing over longer timescales and larger brain areas. Examples are studies of network-level activity, functional connectivity between different cortical areas (Yazdan-Shahmorad *et al.*, 2018; Bloch *et al.*, 2019, 2022) and neurological diseases and disorders.

Conclusion and future directions

Given that not every experiment requires every technology or use-case we present, our platform is functionally modular, providing flexibility to select modalities appropriate for one experiment while maintaining the opportunity to incorporate other modalities in future studies with the same monkey. For

example, an imaging-specific neuropathology study could be followed by development of simultaneous optogenetic and electrical stimulation protocols, which could speed the translation of the new diagnostic or therapeutic techniques from animals to humans. We anticipate wireless closed-loop technologies (Zhou *et al.*, 2019) and next-generation optical and ECoG devices (Belloir *et al.*, 2022; Vargo *et al.*, 2023) will be integrated into designs based on our platform to make our work practical for experimentation on freely moving animals. We expect this to further advance stimulation-based therapies for neurological diseases and disorders (Qiao *et al.*, 2023).

Methods

Our data analysis code and the design files of our electronic and hardware parts are publicly available (https://bitbucket.org/yazdanlab/interface_code/src/main/; https://bitbucket.org/yazdanlab/interface_electronics/src/main/; https://bitbucket.org/yazdanlab/interface_hardware/src/main/).

MMAD

To address tissue growth concerns, we chose to embed a multi-modal artificial dura (MMAD, model "yazdan ecog v10", Ripple Neuro) ECoG array, similar to past work (Devon J Griggs *et al.*, 2021), into a traditional artificial dura (Fig. 1C). Briefly, the MMAD consisted of four conductive layers sandwiched between five transparent layers of medical-grade copolymer, where the conductive layers were aligned with each other to maximize optical access. Conductive layers were composed of platinum particles dispersed in a matrix within the polymer for mechanical flexibility, which was complimented by the absence of printed circuit boards (PCBs). This design choice also side-steps the challenge of protecting PCBs from moisture and fluids. The MMAD was designed in close collaboration with Ripple Neuro (Salt Lake City, UT, USA), who printed the arrays.

A traditional artificial dura is typically described as "top-hat" shaped: a single silicone piece is composed of a cylindrical wall with an optical window at the lower end and a flange extending under the native dura to reduce regrowth of the native dura (Fig. 1C), (Arieli *et al.*, 2002; Ruiz *et al.*, 2013; A Yazdan-Shahmorad *et al.*, 2016). Here, we embedded the MMAD into the artificial dura with a simple, previously described molding process (Griggs *et al.*, 2019; Iritani *et al.*, 2024). Disassembly of the mold resulted in an artificial dura (skirt Ø: 31.2 mm; skirt thickness: 0.4 mm; wall outer Ø: 21.0 mm; wall inner Ø: 18.6 mm; height: 11.9 mm) with a fully embedded MMAD (Fig. 1B).

We designed the entire MMAD, including the cables, as a corrosion resistant single piece. We housed the cables of the MMAD in the chamber between experiments, and during experiments we attached the cables to the electrophysiological recording and stimulation hardware.

Chamber

The chamber is a cylinder (internal Ø 23 mm), 3D-printed and milled from titanium (Ti-6Al-4V, Hybex Innovations, Anjou, Quebec, Canada), which provides a sturdy base for experimental equipment and protects the brain when the monkey is freely moving between experiments, similar to previous work (Azadeh Yazdan-Shahmorad *et al.*, 2016). To design the chamber to fit the skull of each monkey, we developed a software pipeline (MATLAB, MathWorks, Natick, MA, USA; Solidworks, Waltham, MA, USA) to extract the skull curvature from an MRI file and then used the curvature to design a chamber with a unique skull-fitting skirt (Fig. 1A, B; Supp. Fig. 4) (Ojemann *et al.*, 2020; Iritani *et al.*, 2024). We included an intra-cranial rim under the skirt (Supp. Fig. 4) to aid in positioning the chamber on the skull during surgery and to reduce bone growth around the wall of the craniotomy, and we included 12 holes in the skirt (Supp. Fig. 4) for titanium skull tap screws (Christ Instruments, Hagerstown, MD, USA). We

incorporated concentric tracks within the chamber to store the MMAD cables between experiments (Fig. 1B-D). We threaded the chamber with a high thread pitch (M38 × 1.5) to allow either affixation of experimental equipment or a cap to close the chamber between experiments (Fig. 1B; Supp. Fig. 4).

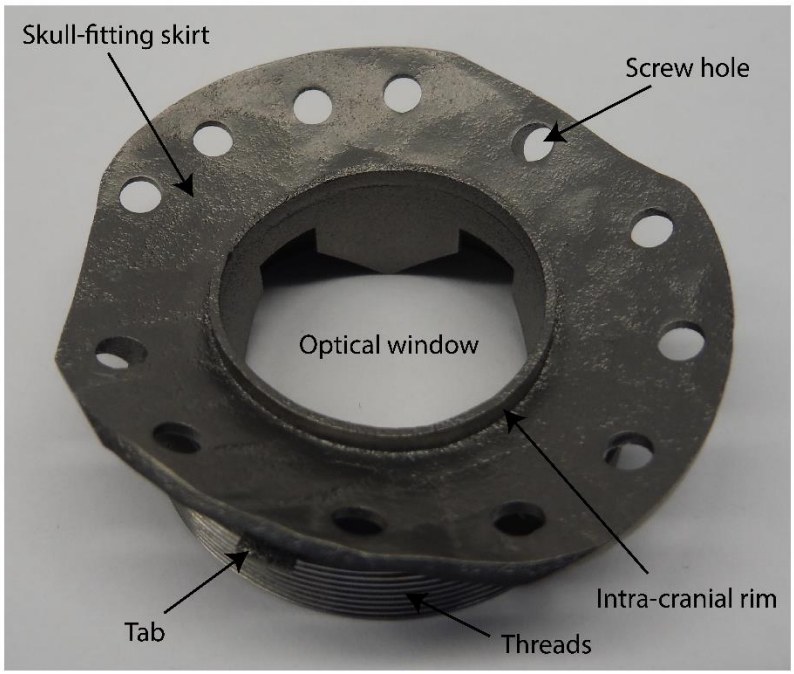

Supp. Fig. 4: Chamber viewed from below skirt.

Cap

We designed a cap (stainless steel 304, machined by Hybex Innovations) to close off the chamber between experiments. We applied polytetrafluoroethylene (PTFE) tape to the threads before each closure to prevent binding of the threads. We used a set screw (HSS11400187HD, #4-40 × 3/16) to fasten the cap shut against the top rim of the chamber.

Electrophysiology hardware

Our electrophysiology setup included a ring, a clamp connector tray, and PCB clamp connectors (Fig. 1E-G). To prepare our platform for recording and stimulation, we screwed the ring onto the chamber and secured the clamp connector tray onto the ring with 2-4 screws (M2.5 × 6). The ring was machined from stainless steel (304; Hybex Innovations) and the clamp connector tray was 3D printed with titanium (TI-64; i.materialise, Leuven, Belgium).

The ring had 32 screw holes (M2.5) around its rim to offer optimal flexibility in the orientation of attachments. The upper face of the ring included a slight recess just above the threads for additional hardware to be easily aligned with the ring for fastening.

The bottom of the clamp connector tray included an intra-ring rim around the window to fit into the recess of the ring. The base of the tray included a right-angled outer rim for grounding electronics as well as four elevated screw holes (M2.5 or 4–40 thread) designed for optical stimulation equipment to be secured to the tray. We designed the tray to be compatible with both this work's LED-based optical stimulation setup and our lab's previously described fiberoptic-based setup (A Yazdan-Shahmorad *et al.*, 2016). We designed the arms of the tray to be low weight and provide support for the MMAD cables as

they extended from the artificial dura walls at 45°. The distal end of the tray arm was approximately 9.5 cm away from the cranial window.

The arms of the tray supported PCB clamp connectors (Fig. 1E-F; Ripple Neuro) held in place by rubber bands (not shown), which secured the MMAD cables approximately 4.5 cm away from the brain and provided an electrical connection between the cables and commercial neurophysiology equipment (Grapevine Nomad, Ripple Neuro). Two of these setups may be simultaneously deployed bilaterally, although this work is exclusive to the left hemisphere.

Optical stimulation hardware

To optically stimulate across large cortical areas (~1 cm^2), we incorporated either a 4 × 4 or a 3 × 5 LED array (Fig. 2). The full 4 × 4 array was used for stimulation during reaches. To prevent LED arrays from moving when in use, we designed a system involving a rod, tube, coverslip, and stimulation holder (Fig. 1G). We custom designed and 3D printed the rod, tube, and stimulation holder in-house with FDM PLA (M2 revG, MakerGear LLC, Beachwood, OH, USA). We glued (Better Ultimate Adhesive, slow dry, Cemedine Co. Ltd., Shinagawa City, Tokyo, Japan) the coverslip (Ø 16 mm, ORSAtec, Bobingen, Germany) to one end of the tube. The base, which we affixed to the clamp connector tray, secured the coverslip against the top side of the MMAD and a set screw (HSS11400187HD, #4–40 × 3/16) secured the rod inside the tube. The rod positioned the LED array over the brain and above the coverslip. Our setup created an air gap between the LEDs and the coverslip, which protected the brain from conductive heating. Four screws in the base secure the tube in place.

The LED array consisted of a circular custom rigid printed circuit board (PCB; Ø 15.5 mm; OSH Park, Portland, OR, USA). The LEDs (L1C1-RED1 or L1C1-BLU1, Lumileds, Schipol, Netherlands) of the 3 × 5 array were individually addressable, while the 4 × 4 array was wired to drive four individually addressable columns of LEDs. Both PCB versions included an internal copper plane for heat dissipation. We soldered the LEDs on one side of the PCB and a connector (501331-0807, Molex Inc., Lisle, IL, USA) on the other side. We drove the LEDs with a custom external PCB (OSH Park) connected to the LED array by a cable assembly (151330806, Molex Inc.). The external PCB consisted of voltage-controlled current sources. Each driving circuit consisted of a high output current opamp (TLE2301, Texas Instruments, Dallas, TX, USA) with a capacitor between the compensation network terminals (not shown) and a resister (15 Ω, 5 W, SMW515RJT, TE Connectivity, Schaffhausen, Switzerland), where the resister value controls the ratio of input voltage to output current. The input voltage is provided by our neurophysiology system's analog voltage output (Ripple Neuro) and is prevented from floating high (e.g., when the neurophysiology system is turned off) by a pull-down resistor (10 kΩ). We powered our PCBs with two in-series batteries (9V Li-ion rechargeable, Keenstone, Industry, CA, USA) to reduce line noise in our electrophysiological recordings. We depict our circuit and arrays in Fig. 2 and Supp. Fig. 1.

We also designed our clamp connector tray to be compatible with our previous laser stimulation setup (Yazdan-Shahmorad *et al.*, 2015), and its slightly modified version is briefly described here. Our setup was composed of a base similar to the base for the LED array setup, and a stimulation ring, both FDM 3D-printed in-house with black PLA. The base was screwed to the clamp connector tray. The stimulation ring guided telescoping cannulas (HTX-13R, HTX-16T, and HTX-18T, Component Supply Co., Sparta, TN, USA) to different stimulation locations, and optical fibers were slid through the cannulas. We coupled lasers (520 nm or 638 nm, LDFLS_520_520_638_638, Doric Lenses, Quebec, Canada) to the optical fibers.

Animals

We recruited two healthy, socially housed male rhesus macaques (*Macaca mulatta*; Monkey H: 9 y, 13 kg; Monkey L: 9 y, 11 kg) for this study. Water was available *ad libitum* and standard food rations were provided after experimental sessions. All animal care and experiments were approved by the University of Washington's Office of Animal Welfare, the Internal Animal Care and Use Committee, and the Washington National Primate Research Center.

Surgical procedures

We performed surgical procedures on both monkeys similar to procedures in other work (A Yazdan-Shahmorad *et al.*, 2016). We sedated the monkey and shaved its head before anesthetizing and head-fixing him in a stereotactic frame. The respiratory rate, heart rate, and body temperature of the monkey were monitored throughout the procedure. We created an incision several cm long to the left of the head's midline and used elevators to peel back the skin, musculature, and muscle fascia. We confirmed the location of the center of the craniotomy with stereotactic coordinates. Using a Ø 25-mm trephine, we created the craniotomy. Then we resected the dura by lifting the dura with a curved needle and trimming with ophthalmic scissors, revealing the posterior parietal cortex. After test-fitting the titanium chamber to the skull, we placed a flat transparent silicone artificial dura on the brain to keep the brain moist.

With the craniotomy complete, we performed convection-enhanced delivery (CED) of Jaws (rAAV8/hSyn-Jaws-KGC-GFP-ER2, 5.4 x 10^{12} virus molecules/mL, University of North Carolina Vector Core), a red-shifted inhibitory viral vector (Chuong *et al.*, 2014). Prior to surgery, we had manufactured a 1-mm stepped-tip silica cannula (inner cannula: inner Ø 320 µm, outer Ø 435 µm; outer cannula: inner Ø 450 µm, outer Ø 673 µm; Polymicro Technologies, Phoenix, AZ, USA) for CED similar to our previous work (A Yazdan-Shahmorad *et al.*, 2016; Griggs *et al.*, 2022b) by applying cyanoacrylate (super glue) to the inner cannula, sliding the outer cannula over the inner cannula, and using a razor blade to trim the inner cannula extending from one side of the outer cannula to make a 1-mm stepped-tip. We removed the artificial dura from the brain, punched a hole through the artificial dura to be used for our injection, laid the artificial dura back on the brain to keep the brain moist, and then inserted the cannula tip through the hole approximately 2 mm into the cortex (Fig. 3A, top left) and began the infusion protocol similar to previous work (A Yazdan-Shahmorad *et al.*, 2016). We infused up to 50 µL at each of several locations across the cortex. Once complete, we placed a new artificial dura on the brain.

Unlike previous work where live-MRI was performed during infusions (A Yazdan-Shahmorad *et al.*, 2016; Karam Khateeb *et al.*, 2019), we performed the infusions without live-MRI. This allowed CED to be performed in the surgery suite while we were able to visually inspect the location of infusion for any reflux. It is also eliminated the need for MRI-compatible syringe pumps or complicated fluid line setups – the syringe and cannula were attached directly to the pump, and a stereotactic arm was used for cannula insertion during CED.

Following CED, we placed the chamber on the skull. We used a piezo-drill (5120063AS animal science package, insert tips IM1-AL and IM1S, Piezosurgery Inc., Columbus, OH) to drill screw holes and used titanium tap screws (Crist Instruments) to secure the chamber to the skull. We removed the artificial dura and placed the MMAD on the brain and housed the cables in the slots of the chamber (Fig. 1D). Finally, we applied PTFE tape to the threads, closed the cap, secured the set screw, and applied bone wax to the set screw. Having secured and closed the chamber, we closed the wound using standard surgical techniques.

We had implanted a titanium headpost (Crist Instruments) on each monkey prior to this study (Ojemann *et al.*, 2020).

Chamber cleaning and hardware assembly

We developed a process of cleaning the chamber at least three times each week, starting one week after the surgery. We briefly describe the processes here. After head-fixing the monkey, we cleaned the cap, chamber margin, surrounding scalp and outside of the ear. Once clean, we removed the cap and cleaned the margin. We used cotton-tipped applicators dipped in saline to clean the threads and the rim of the chamber. To clean the inside of the chamber, we used a sterile syringe and blunt-tipped needle to irrigate warm saline on and in the MMAD, its cables, and the storage area for the cables.

To prepare for electrophysiological recording, we screwed a sterile ring onto the chamber and screwed a sterile clamp connector tray to the ring with sterile screws. Then we removed the cables from the chamber and placed them into the clamp connectors, and rubber banded the clamp connectors to the clamp connector tray arms.

To prepare for optical stimulation, we attached the stimulation holder for either the LED array or for the lasers. In the case of laser stimulation, we slid the stimulation ring down around the stimulation holder and we inserted the fiberoptic cable through the cannula and cannula through the simulation ring. In the case of LED stimulation, we assembled the LED array, rod, and tube with coverslip, and secured them together with a set screw. Then we lowered the assembly down through the stimulation holder and into the MMAD, and secured the tube into place with set screws. Black foil was wrapped around the stimulation equipment to prevent the monkey from seeing any lighting changes in the experimental rig due to stimulation.

When the experiment was complete, we removed the stimulation and recording equipment, cleaned the MMAD, and used forceps to return the cables back into the chamber. Then we cleaned the chamber using saline irrigation and applied antibiotic to the center of the MMAD. To avoid building antibiotic resistance, we rotated through polymyxin B sulfate, gentamicin, and amikacin sulfate antibiotics, applying one for 4-5 weeks and then switching to the next. To prevent the cap from binding to the chamber between cleanings, we wrapped a strip of sterile PTFE around a portion of the threads. Then we screwed on a sterile cap and a set screw.

Epifluorescence imaging

We performed epifluorescence imaging of green fluorescence protein (GFP) by using a blue light for the excitation wavelength of GFP (NIGHTSEA stereo microscope fluorescence adapter, SFA-RB royal blue, Electron Microscopy Sciences, Hatfield, PA) in front of a DLSR camera (Nikon D5300, Minato City, Tokyo, Japan) and used a lens based on the emission wavelength of the GFP (Nikon DX AF-S NIKKOR 35mm 1:1.8G, SWM Aspherical ∞-0.3m/0.98ft Ø52). We illuminated the brain from multiple angles to fully cover the optical window. The camera was fixed throughout the illumination process, which eased stitching the photos together with image editing software.

Behavioral task

Our a center-out reach task (Fig. 4A) was controlled by a custom software in MATLAB using Psychophysics Toolbox version 3 (Brainard, 1997; Pelli, 1997; Kleiner *et al.*, 2007), similar to previous work (Griggs *et al.*, 2020). A reflective sticker, placed on the middle finger of the monkey's right hand, contralateral to the implant, was tracked by a motion capture system (Motive, OptiTrack, NaturalPoint

Inc., Corvallis, OR, USA). These tracking data were processed in real-time by MATLAB. The monkey was rewarded for successful trials with juice (5-RLD-D1 D.A.R.I.S., Crist Instruments). The monkey was head-fixed and seated in a monkey chair inside a dark experimental rig. The visual and audio stimuli were provided by a monitor with built-in speakers within reaching distance of the monkey.

Monkeys performed several hundred trials each session (monkey H: mean trials per session: 557.7, standard deviation: 217.6, total trials across sessions: 3904; monkey L: mean trials per session: 715.7, standard deviation: 266.0, total trials across sessions: 8588). For monkey H, there were 3904 analyzed reach trials split over 7 sessions, while for monkey L there were 8588 trials split over 12 sessions.

Behavioral analysis

We analyzed reach times from the behavioral trials. All successful trials from all sessions were labeled with reach direction (right, down, left, or up) and stimulation condition (stimulation or no stimulation). Data groups were compared statistically by Mann-Whitney U-test of the distribution of reach times.

We tracked the reach path and reach time and analyzed movement in three-dimensional space (two dimensions shown in Fig. 6B-C) for both stimulation and control (no stimulation) conditions. We measured the time between the go-tone and the finger's entry into the end target, and we call this time the "total time." The total time is the sum of two parts, being the time taken for the monkey's finger to exit the start target after the go-tone, which we call the "reaction time," and the time taken to complete the reach from that point, which we call the "movement time."

Behavioral data preprocessing

All reach trials were aggregated over all dates and conditions for both monkeys individually. Trials were excluded from analysis if the reach was unsuccessful or if the trail was a warmup trial as judged from a wait time before the go-tone <0.3 s, or a circle size >50 pixels radius (approx. 25 mm diameter). The counts of included trials are listed in Supp. Table 1.

The neural data were screened to remove malfunctioning electrodes by measuring the impedance of the electrodes and by visual inspection of the voltage traces. Additionally, the standard deviation of the raw neural signal was computed for each trial, and if the z-score of the standard deviation was >6, the trial was excluded.

Supp. Table 1: Total successful trial counts.

	Monkey H Trials, Stimulation	Monkey H Trials, Control	Monkey L Trials, Stimulation	Monkey L Trials, Control
Right	473	484	971	1049
Down	471	501	987	1090
Left	477	509	1060	1141
Up	466	523	1073	1073
Total	1976	1928	4194	4394

Neural data analysis

Neural activity was recorded during behavior and stimulation (1 kHz sampling frequency, Grapevine Nomad, Ripple Neuro). All neural data analyses were conducted separately for the two monkeys.

The process involved segregating all trials into stimulation and non-stimulation trials. Each trial was then split into three epochs: before stimulation, during stimulation, and after stimulation. During the "before stimulation" period, we analyzed the 500 ms of LFP immediately before stimulation began. The "during stimulation" period corresponded to the LFP recorded during the 900 ms stimulation, excluding the first 50 ms of the stimulation. The "after stimulation" period corresponded to the 900 ms following the end of the stimulation, excluding the first 50 ms. Exclusion of these 50-ms windows of LFP was driven by the challenges associated with removing artifacts during these specific periods. Time-series of included data were subsequently analyzed in 50 ms windows and then averaged within epochs, obtaining high time-resolution and enabling the comparison of epochs of different total lengths. We applied artifact removal to each epoch (see below).

We first removed photo-induced artifact and then quantified the effect of stimulation on reaching neural activity by analyzing the time-frequency content of the data (Fig. 7). The trials were grouped by monkey and by condition, i.e., control and stimulated reaches. ECoG data from each trial were analyzed in the time-frequency domain via multitaper spectrograms. The average spectrogram for a reach in the presence of stimulation is shown in Figs. 7A and 7E, and the average spectrogram for a control reach is shown in Figs. 7B and 7F. In these figures, the values are normalized by the pre-stimulation activity such that the average pre-stimulation activity is unity for each individual frequency. Vertical grey bars indicate the start and termination of stimulation. The 50 ms immediately following the start and termination of stimulation are excluded to avoid including any residual artifact in the signal at these times. To quantify modulation, we calculated the power ratios of the spectrograms from the stimulated to the control trials (Fig. 7C and 7G). The 500-ms time period before stimulation was used to calculate the average power in each frequency bin. These averages were then used to normalize the power in the corresponding frequency bins following stimulation onset.

Photo-induced artifact removal

To isolate photo-induced artifacts from the electrocorticography acquired during simultaneous optical stimulation *in vivo*, we generated a dataset of these artifacts, absent any neural signals, by optically stimulating an electrode array submerged in a saline bath. We modeled the photo-induced artifact using these saline data, fit the model to the *in vivo* electrocorticography, and removed the estimated photo-induced artifact. The procedure involved the following steps (Supp. Fig. 5A-D):

1. The time surrounding each stimulation in the saline data was isolated, from 100 ms before the onset of stimulation to one second after the end of stimulation. Each of the 32 channels were stacked with their 100 corresponding stimulation pulses to form a matrix (32 × 100 × length of time).

2. The matrix was split along the time axis into three matrices corresponding to before stimulation, during stimulation, and after stimulation.

3. The saline data at the time of stimulation onset and offset (data point *time = 0* for matrices "during stimulation" and "after stimulation," respectively) were set to 0 mV and the whole traces were shifted accordingly.

4. Photo-induced artifact was modeled from these data using principal component analysis (PCA) conducted separately on the "during stimulation" and "after stimulation" matrices, with the top three components extracted from each.

This model was subsequently employed to eliminate the artifact from the *in vivo* data as follows:

5. The *in vivo* data was isolated and stacked in the same way as the saline data, such that a data matrix (channels × pulses × length of time), with identical time length, was formed.
6. The matrix was split along the time axis into three matrices corresponding to before stimulation during stimulation, and after stimulation.
7. The ECoG data at the time of stimulation onset and offset (data point *time = 0* for matrices "during stimulation" and "after stimulation") were set to 0 mV and the whole traces were shifted accordingly.
8. The ECoG data from the "during stimulation" and "after stimulation" matrices were projected onto the corresponding models derived from saline, and the estimated photo-induced artifact was regressed out of the NHP data using linear regression.
9. The three matrices were rejoined along the time axis, adding an offset to the later matrices such that the average LFP value of the last 50 ms of the preceding matrix and the first 50 ms of the later matrix had the same average value.

This procedure enabled the separation of the photo-induced artifact from neural activity, and retaining the neural activity in the recorded signal (Supp. Fig. 5E), as confirmed by controls (Supp. Fig. 5F).

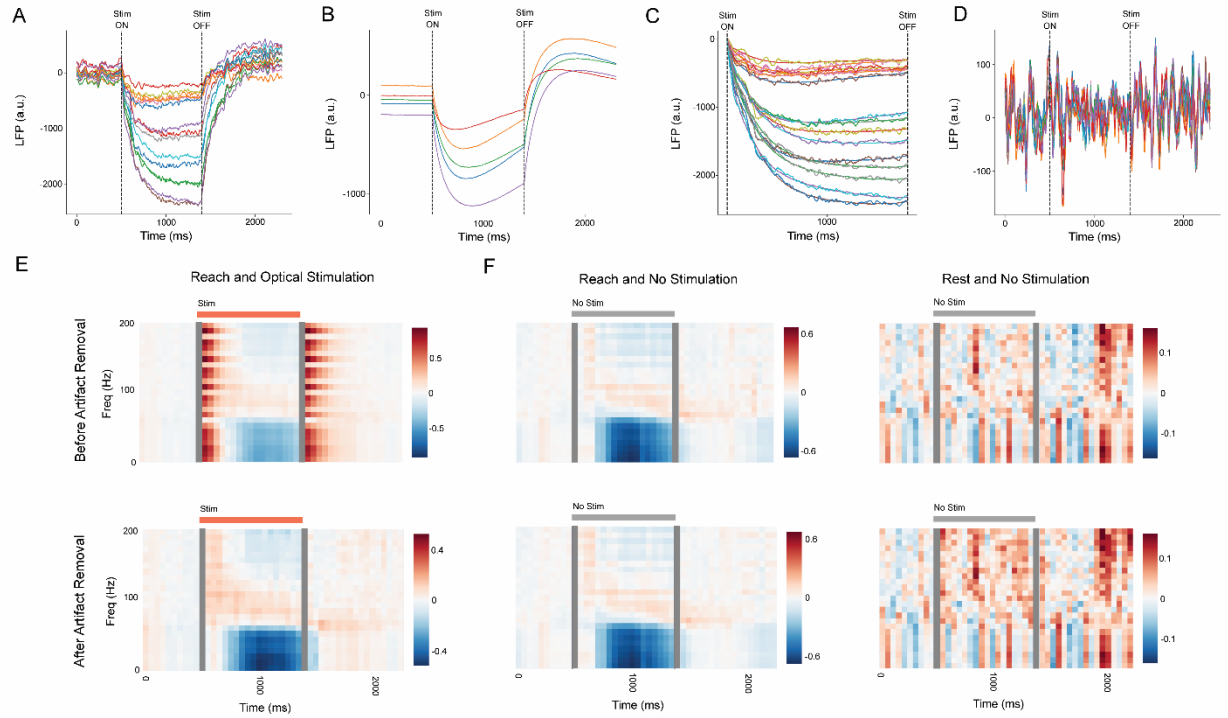

Supp. Fig. 5: Removal of light-induced artifact. ***(A)*** *LFP timeseries during optical stimulation of cortex.* ***(B)*** *Recording during optical stimulation of ECoG array in a saline bath.* ***(C)*** *Neural recordings overlaid with a reconstructed artifact template found by projecting the recording into the first four principal components of saline recording.* ***(D)*** *LFP timeseries with photo-artifact removed using the reconstructed artifact template.* ***(E)*** *Spectrograms of LFP data before (top) and after (bottom) artifact*

removal under optical stimulation, during reach. ***(F)*** *As controls, signals without optical stimulation were passed through the artifact removal process. Spectrograms of LFP data before (top) and after (bottom) artifact removal of control signals without optical stimulation, during reach (left) and rest (right). Note the reduced magnitude of the color bar of the rest condition in comparison to the reach conditions.*

Time-frequency analysis

We analyzed neural activity in the time-frequency domain by generating spectrograms using multitaper-based analysis of 50-ms non-overlapping windows. Five tapers were used, with a 128-sample length Fast Fourier Transform (FFT) between 1-200Hz. The 50 ms immediately after stimulation onset and offset were excluded from analysis. Spectrograms were normalized to the 500 ms of activity preceding stimulation, on a trial-by-trial for each frequency bin. For every channel of every trial, each frequency bin was divided by the average power in that frequency bin 500 ms before stimulation. For the control condition (not stimulated), the same normalization was performed using 500 ms before stimulation would have occurred.

To quantify the changes due to stimulation when the animal was at rest, we calculated the average values of the spectrogram per frequency bin. Since the spectrograms (which are power ratios) were normalized to the 500 ms preceding stimulation, statistical differences induced by stimulation in neural activity were found by comparing the evoked power ratio to 1.

During behavior, broadband power was calculated for the period preceding the end target shown (500 ms), during reaching (900 ms), and after reaching (900 ms). In stimulated trials, the stimulation was time locked to the presentation of the end target. Statistical differences in neural activity induced by stimulation during reaching were found by comparing the broadband power in the control condition to the broadband power in the stimulated condition for each epoch of activity using the Mann Whitney U test.

For spectrograms depicting the time-frequency ratios of stimulated to control condition, the spectrograms for the stimulated and control conditions were calculated and averaged over all trials and channels and sessions. Distributions of time-frequency bins in the stimulated and control conditions were compared via paired t-test. To account for multiple comparisons and mitigate the risk of Type I errors, a Bonferroni correction was applied *post hoc*.

Acknowledgment

We thank Zachary Ip and William Ojemann for their help with MRI processing; William Ojemann, Kali Coubrough, Jia Wen Chan, Karam Khateeb, Zada Anderson, Stephen Philips, and Andrew Graham Johnson for their help with part design; Ripple Neuro, especially Alex Johnson, Jose Ortega, and Jessi Michel, for their help with designing and manufacturing the MMADs; Karam Khateeb and William Ojemann for their help with MMAD molding; Marcus Chu and Mona Rahimi for their help with electronics; Kelly Morrisroe, Tiphaine Belloir, Kelly Yeh, Toni Haun, Briana Smith, Kali Coubrough, Shivalika Chavan, Pavi Rajeswaran, Kiara Evitts, and Avi Matarasso for their help with animal training; Jane Sullivan for her help with opsin validation prior to infusion; Greg Horwitz, Keith Vogel, Toni Haun, Karam Khateeb, Zachary Ip, and WaNPRC veterinarians and staff for their help with surgeries; Tiphaine Belloir, Kelly Yeh, Toni Haun, and WaNPRC veterinarians and staff for their help with chamber care; Kali Coubrough and Shivalika Chavan for their help with behavioral rig development; Ryan Ressmeyer and Arie Aelmore for their help with data analysis.

We thank our funding sources: R01 NS119395 (DJG, JB, JZ, AY), R01 NS116464-01 (AY), University of Washington Big Data for Genomics & Neuroscience Training Grant (JB), Weill Neurohub (SF), Washington National Primate Research Center P51 OD010425 (DJG, JB, NS, JZ, SF, AY), American Heart Association (AY), 1T32 MH132518 (NS), R01 MH125429 (NS, AY), and K01 AG071798 (HJ).

References

Acker, L., Pino, E. N., Boyden, E. S. and Desimone, R. (2016) 'FEF inactivation with improved optogenetic methods', *Proc Natl Acad Sci U S A*. 2016/11/04, 113(46), pp. E7297–E7306. doi: 10.1073/pnas.1610784113.

Adhikari, A., Lerner, T. N., Finkelstein, J., Pak, S., Jennings, J. H., Davidson, T. J., Ferenczi, E., Gunaydin, L. A., Mirzabekov, J. J., Ye, L., Kim, S. Y., Lei, A. and Deisseroth, K. (2015) 'Basomedial amygdala mediates top-down control of anxiety and fear', *Nature*, 527(7577), pp. 179–185. doi: 10.1038/nature15698.

Arieli, A., Grinvald, A. and Slovin, H. (2002) 'Dural substitute for long-term imaging of cortical activity in behaving monkeys and its clinical implications', *Journal of Neuroscience Methods*, 114(2), pp. 119–133. doi: 10.1016/S0165-0270(01)00507-6.

Barnett, S. C., Perry, B. A. L., Dalrymple-Alford, J. C. and Parr-Brownlie, L. C. (2018) 'Optogenetic stimulation: Understanding memory and treating deficits', *Hippocampus*, 28(7), pp. 457–470. doi: 10.1002/hipo.22960.

Belloir, T., Belloir, T., Vargo, S. M., Ahmed, Z., Griggs, D., Fisher, S., Brown, T., Chamanzar, M. and Yazdan-shamorad, A. (2022) 'iScience Large-scale multimodal surface neural interfaces for non-human primates', *ISCIENCE*.

Bloch, J. (2023) *Computational and Experimental Advances in Clinically Relevant Neurostimulation of Non-Human Primates*, *ProQuest Dissertations and Theses*. University of Washington PP - United States -- Washington. Available at: https://www.proquest.com/dissertations-theses/computational-experimental-advances-clinically/docview/2915766719/se-2?accountid=14505.

Bloch, J. A., Khateeb, K., Silversmith, D. B., O'Doherty, J. E., Sabes, P. N. and Yazdan-Shahmorad, A. (2019) 'Cortical Stimulation Induces Network-Wide Coherence Change in Non-Human Primate Somatosensory Cortex∗', *Proceedings of the Annual International Conference of the IEEE Engineering in Medicine and Biology Society, EMBS*, pp. 6446–6449. doi: 10.1109/EMBC.2019.8856633.

Bloch, J., Shea-brown, E., Harchaoui, Z. and Shojaie, A. (2022) 'iScience ll Network structure mediates functional reorganization induced by optogenetic stimulation of non-human primate sensorimotor cortex', *ISCIENCE*, 25(5), p. 104285. doi: 10.1016/j.isci.2022.104285.

Brainard, D. H. (1997) 'The Psychophysics Toolbox', *Spatial Vision*, 10(4), pp. 433–436.

Camporeze, B., Manica, B. A., Bonafé, G. A., Ferreira, J. J. C., Diniz, A. L., de Oliveira, C. T. P., Mathias Junior, L. R., de Aguiar, P. H. P. and Ortega, M. M. (2018) 'Optogenetics: the new molecular approach to control functions of neural cells in epilepsy, depression and tumors of the central nervous system.', *American journal of cancer research*, 8(10), pp. 1900–1918. Available at: http://www.ncbi.nlm.nih.gov/pubmed/30416844%0Ahttp://www.pubmedcentral.nih.gov/articlerender.fcgi?artid=PMC6220144.

Carter, M. E. and de Lecea, L. (2011) 'Optogenetic investigation of neural circuits in vivo', *Trends in Molecular Medicine*, 17(4), pp. 197–206. doi: 10.1016/j.molmed.2010.12.005.

Chen, B. T., Yau, H. J., Hatch, C., Kusumoto-Yoshida, I., Cho, S. L., Hopf, F. W. and Bonci, A. (2013) 'Rescuing cocaine-induced prefrontal cortex hypoactivity prevents compulsive cocaine seeking', *Nature*, 496(7445), pp. 359–362. doi: 10.1038/nature12024.

Chen, L. M., Heider, B., Williams, G. V., Healy, F. L., Ramsden, B. M. and Roe, A. W. (2002) 'A chamber and artificial dura method for long-term optical imaging in the monkey', *Journal of Neuroscience*

Methods, 113(1), pp. 41–49. doi: 10.1016/S0165-0270(01)00475-7.

Chernov, M. and Roe, A. W. (2014) 'Infrared neural stimulation: a new stimulation tool for central nervous system applications', *Neurophotonics*, 1(1), p. 011011. doi: 10.1117/1.nph.1.1.011011.

Chiang, C.-H., Won, S. M., Orsborn, A. L., Yu, K. J., Trumpis, M., Bent, B., Wang, C., Xue, Y., Min, S., Woods, V., Yu, C., Kim, B. H., Kim, S. B., Huq, R., Li, J., Seo, K. J., Vitale, F., Richardson, A., Fang, H., *et al.* (2020) 'Development of a neural interface for high-definition, long-term recording in rodents and nonhuman primates', *Science Translational Medicine*, 12(538), p. eaay4682. doi: 10.1126/scitranslmed.aay4682.

Chuong, A. S., Miri, M. L., Busskamp, V., Matthews, G. A. C., Acker, L. C., Sørensen, A. T., Young, A., Klapoetke, N. C., Henninger, M. A., Kodandaramaiah, S. B., Ogawa, M., Ramanlal, S. B., Bandler, R. C., Allen, B. D., Forest, C. R., Chow, B. Y., Han, X., Lin, Y., Tye, K. M., *et al.* (2014) 'Noninvasive optical inhibition with a red-shifted microbial rhodopsin', *Nature Neuroscience*, 17(8), pp. 1123–1129. doi: 10.1038/nn.3752.

Diester, I., Kaufman, M. T., Mogri, M., Pashaie, R., Goo, W., Yizhar, O., Ramakrishnan, C., Deisseroth, K. and Shenoy, K. V. (2011) 'An optogenetic toolbox designed for primates', *Nature Neuroscience*, 14(3), pp. 387–397. doi: 10.1038/nn.2749.

Gradinaru, V., Mogri, M., Thompson, K. R., Henderson, J. M. and Deisseroth, K. (2009) 'Optical deconstruction of parkinsonian neural circuitry', *Science*, 324(5925), pp. 354–359. doi: 10.1126/science.1167093.

Griggs, D. J. (2022) *Accessible Optogenetic Technologies for Non-Human Primate Research*, *ProQuest Dissertations and Theses*. University of Washington PP - United States -- Washington. Available at: https://www.proquest.com/dissertations-theses/accessible-optogenetic-technologies-non-human/docview/2719410137/se-2?accountid=14505.

Griggs, Devon J., Belloir, T. and Yazdan-Shahmorad, A. (2021) 'Large-scale neural interfaces for optogenetic actuators and sensors in non-human primates', *SPIE BiOS*, 1166305(March), p. 17. doi: 10.1117/12.2579431.

Griggs, D. J., Bloch, J., Chavan, S., Coubrough, K. M., Conley, W., Morrisroe, K. and Yazdan-Shahmorad, A. (2020) 'Autonomous cage-side system for remote training of non-human primates', *Journal of Neuroscience Methods*, 348(October 2020), p. 108969. doi: 10.1016/j.jneumeth.2020.108969.

Griggs, D. J., Bloch, J., Fisher, S., Ojemann, W. K. S., Coubrough, K. M., Chu, M. and Yazdan-shahmorad, A. (2022a) 'Demonstration of an Optimized Large-scale Optogenetic Cortical Interface for Non-human Primates', *Ieee*, 119395, pp. 1–4.

Griggs, D. J., Garcia, A. D., Au, W. Y., Ojemann, W. K. S., Johnson, A. G., Ting, J. T., Buffalo, E. A. and Yazdan-Shahmorad, A. (2022b) 'Improving the efficacy and accessibility of intracranial viral vector delivery in non-human primates', *Pharmaceutics*, p. 2022.06.06.494543. doi: 10.1101/2022.06.06.494543.

Griggs, D. J., Khateeb, K., Philips, S., Chan, J. W., Ojemann, W., Yazdan-Shahmorad, A., D. J. Griggs S. Philips, J. W. Chan, W.K.S. Ojemann, A. Yazdan-Shahmorad, K. K., Griggs, D. J., Khateeb, K., Philips, S., Chan, J. W., Ojemann, W. and Yazdan-Shahmorad, A. (2019) 'Optimized large-scale optogenetic interface for non-human primates', *SPIE BiOS*, 1086605(February), p. 3. doi: 10.1117/12.2511317.

Griggs, Devon J, Khateeb, K., Zhou, J., Liu, T., Wang, R. and Yazdan-Shahmorad, A. (2021) 'Multi-modal artificial dura for simultaneous large-scale optical access and large-scale electrophysiology in non-human primate cortex', *Journal of Neural Engineering, Special Issue 'Neuroelectronic Interfaces'*, 18(5), p. 2021.02.03.429596. doi: 10.1101/2021.02.03.429596.

Han, X., Qian, X., Bernstein, J. G., Zhou, H., Franzesi, G., Stern, P., Bronson, R., Graybiel, A., Desimone, R. and Boyden, E. S. (2009) 'Millisecond-Timescale Optical Control of Neural Dynamics in the Nonhuman

Primate Brain', *Neuron*, 62(2), pp. 191–198. Available at: doi:10.1016/j.neuron.2009.03.011.

Hart, W. L., Richardson, R. T., Kameneva, T., Thompson, A. C., Wise, A. K., Fallon, J. B., Stoddart, P. R. and Needham, K. (2020) 'Combined optogenetic and electrical stimulation of auditory neurons increases effective stimulation frequency - An in vitro study', *Journal of Neural Engineering*, 17(1). doi: 10.1088/1741-2552/ab6a68.

Iritani, R., Belloir, T., Griggs, D. J., Ip, Z., Anderson, Z. and Yazdan-Shahmorad, A. (2024) 'A Neural Implant Design Toolbox for Nonhuman Primates', *Journal of Visualized Experiments*. doi: http://dx.doi.org/10.3791/66167.

Jacques, S. L. (2013) 'Erratum: Optical properties of biological tissues: A review (Physics in Medicine and Biology (2013) 58)', *Physics in Medicine and Biology*, 58(14), pp. 5007–5008. doi: 10.1088/0031-9155/58/14/5007.

Ji, B., Guo, Z., Wang, M., Yang, B., Wang, X., Li, W. and Liu, J. (2018) 'Flexible polyimide-based hybrid opto-electric neural interface with 16 channels of micro-LEDs and electrodes', *Microsystems and Nanoengineering*, 4(1). doi: 10.1038/s41378-018-0027-0.

Jiang, W., Tremblay, F. and Elaine Chapman, C. (2018) 'Context-dependent tactile texture-sensitivity in monkey M1 and S1 cortex', *Journal of Neurophysiology*, 120(5), pp. 2334–2350. doi: 10.1152/jn.00081.2018.

Khanna, P., Totten, D., Novik, L., Roberts, J., Morecraft, R. J. and Ganguly, K. (2021) 'Low-frequency stimulation enhances ensemble co-firing and dexterity after stroke', *Cell*, 184(4), pp. 912-930.e20. doi: 10.1016/j.cell.2021.01.023.

Khateeb, K., Bloch, J., Zhou, J., Rahimi, M., Griggs, D. J., Kharazia, V. N., Le, M. N., Wang, R. K. and Yazdan-Shahmorad, A. (2022) 'A versatile toolbox for studying cortical physiology in primates', *Cell Reports Methods*, p. 100183. doi: 10.1016/j.crmeth.2022.100183.

Khateeb, Karam, Griggs, D. J., Sabes, P. N. and Yazdan-Shahmorad, A. (2019) 'Convection Enhanced Delivery of Optogenetic Adeno-associated Viral Vector to the Cortex of Rhesus Macaque Under Guidance of Online MRI Images', *J Vis Exp*. 2019/06/11, (147), pp. 1–8. doi: 10.3791/59232.

Khateeb, K, Yao, Z., Kharazia, V. N., Burunova, E. P., Song, S., Wang, R. and Yazdan-Shahmorad, A. (2019) 'A Practical Method for Creating Targeted Focal Ischemic Stroke in the Cortex of Nonhuman Primates(.)', *Conf Proc IEEE Eng Med Biol Soc*. 2020/01/18, 2019, pp. 3515–3518. doi: 10.1109/EMBC.2019.8857741.

Kleiner, M., Brainard, D. H. and Pelli, D. G. (2007) 'What's new in Psychtoolbox-3?', in *Perception 36 ECVP Abstract Supplement*.

Komatsu, M., Sugano, E., Tomita, H. and Fujii, N. (2017) 'A chronically implantable bidirectional neural interface for non-human primates', *Frontiers in Neuroscience*, 11(SEP), pp. 1–9. doi: 10.3389/fnins.2017.00514.

Kooijmans, R. N., Sierhuis, W., Self, M. W. and Roelfsema, P. R. (2020) 'A Quantitative Comparison of Inhibitory Interneuron Size and Distribution between Mouse and Macaque V1, Using Calcium-Binding Proteins', *Cerebral Cortex Communications*, 1(1), pp. 1–14. doi: 10.1093/texcom/tgaa068.

Krauze, M. T., Saito, R., Noble, C., Tamas, M., Bringas, J., Park, J. W., Berger, M. S. and Bankiewicz, K. (2005) 'Reflux-free cannula for convection-enhanced high-speed delivery of therapeutic agents', *J Neurosurg*. 2005/11/25, 103(5), pp. 923–929. doi: 10.3171/jns.2005.103.5.0923.

Lear, A., Baker, S. N., Clarke, H. F., Roberts, A. C., Schmid, M. and Jarrett, W. (2022) 'Understanding them to understand ourselves: The importance of NHP research for translational neuroscience', *Current Research in Neurobiology*, p. 100049.

Macknik, S. L., Alexander, R. G., Caballero, O., Chanovas, J., Nielsen, K. J., Nishimura, N., Schaffer, C. B., Slovin, H., Babayoff, A., Barak, R., Tang, S., Ju, N., Yazdan-Shahmorad, A., Alonso, J. M., Malinskiy, E. and Martinez-Conde, S. (2019) 'Advanced Circuit and Cellular Imaging Methods in Nonhuman Primates', *J*

Neurosci. 2019/10/18, 39(42), pp. 8267–8274. doi: 10.1523/JNEUROSCI.1168-19.2019.

Meyer, H. S., Schwarz, D., Wimmer, V. C., Schmitt, A. C., Kerr, J. N. D., Sakmann, B. and Helmstaedter, M. (2011) 'Inhibitory interneurons in a cortical column form hot zones of inhibition in layers 2 and 5A', *Proceedings of the National Academy of Sciences of the United States of America*, 108(40), pp. 16807–16812. doi: 10.1073/pnas.1113648108.

O'Shea, D. J., Duncker, L., Goo, W., Sun, X., Vyas, S., Trautmann, E. M., Diester, I., Ramakrishnan, C., Deisseroth, K., Sahani, M. and Shenoy, K. V (2022) 'Direct neural perturbations reveal a dynamical mechanism for robust computation', *bioRxiv*, p. 2022.12.16.520768. doi: 10.1101/2022.12.16.520768.

Ohayon, S., Grimaldi, P., Schweers, N. and Tsao, D. Y. (2013) 'Saccade modulation by optical and electrical stimulation in the macaque frontal eye field', *Journal of Neuroscience*, 33(42), pp. 16684–16697. doi: 10.1523/JNEUROSCI.2675-13.2013.

Ojemann, W. K. S., Griggs, D. J., Ip, Z., Caballero, O., Jahanian, H., Martinez-Conde, S., Macknik, S. and Yazdan-Shahmorad, A. (2020) 'A mri-based toolbox for neurosurgical planning in nonhuman primates', *Journal of Visualized Experiments*, 2020(161), pp. 1–16. doi: 10.3791/61098.

Pelli, D. G. (1997) 'The VideoToolbox software for visual psychophysics: Transforming numbers into movies', *Spatial Vision*, 10(4), pp. 437–442.

Qiao, N., Ma, L., Zhang, Y. and Wang, L. (2023) 'Update on Nonhuman Primate Models of Brain Disease and Related Research Tools', *Biomedicines*, 11(9), p. 2516.

Rajalingham, R., Sorenson, M., Azadi, R., Bohn, S., DiCarlo, J. J. and Afraz, A. (2021) 'Chronically implantable LED arrays for behavioral optogenetics in primates', *Nature Methods*, 18(9), pp. 1112–1116. doi: 10.1038/s41592-021-01238-9.

Reddy, J. W., Kimukin, I., Towe, E. and Chamanzar, M. (2019) 'Flexible, Monolithic, High-Density µlED Neural Probes for Simultaneous Optogenetics Stimulation and Recording', *International IEEE/EMBS Conference on Neural Engineering, NER*, 2019-March, pp. 831–834. doi: 10.1109/NER.2019.8717116.

Renz, A. F., Lee, Jihyun, Tybrandt, K., Brzezinski, M., Lorenzo, D. A., Cerra Cheraka, M., Lee, Jaehong, Helmchen, F., Vörös, J. and Lewis, C. M. (2020) 'Opto-E-Dura: A Soft, Stretchable ECoG Array for Multimodal, Multiscale Neuroscience', *Advanced Healthcare Materials*, 9(17), pp. 1–11. doi: 10.1002/adhm.202000814.

Richner, T. J., Thongpang, S., Brodnick, S. K., Schendel, A. A., Falk, R. W., Krugner-Higby, L. A., Pashaie, R. and Williams, J. C. (2014) 'Optogenetic micro-electrocorticography for modulating and localizing cerebral cortex activity', *Journal of Neural Engineering*, 11(1). doi: 10.1088/1741-2560/11/1/016010.

Roelfsema, P. R. and Treue, S. (2014) 'Basic neuroscience research with nonhuman primates: A small but indispensable component of biomedical research', *Neuron*. doi: 10.1016/j.neuron.2014.06.003.

Ruggiero, R. N., Rossignoli, M. T., De Ross, J. B., Hallak, J. E. C., Leite, J. P. and Bueno-Junior, L. S. (2017) 'Cannabinoids and vanilloids in schizophrenia: Neurophysiological evidence and directions for basic research', *Frontiers in Pharmacology*, 8(JUN), pp. 1–27. doi: 10.3389/fphar.2017.00399.

Ruiz, O., Lustig, B. R., Nassi, J. J., Cetin, A., Reynolds, J. H., Albright, T. D., Callaway, E. M., Stoner, G. R. and Roe, A. W. (2013) 'Optogenetics through windows on the brain in the nonhuman primate', *J Neurophysiol*. 2013/06/14, 110(6), pp. 1455–1467. doi: 10.1152/jn.00153.2013.

Schwock, F., Bloch, J., Khateeb, K., Zhou, J., Atlas, L. and Yazdan-Shahmorad, A. (2024) 'Inferring Neural Communication Dynamics from Field Potentials Using Graph Diffusion Autoregression', *bioRxiv*, p. 2024.02.26.582177. doi: 10.1101/2024.02.26.582177.

Slovin, H., Arieli, A., Hildesheim, R. and Grinvald, A. (2002) 'Long-term voltage-sensitive dye imaging reveals cortical dynamics in behaving monkeys', *Journal of Neurophysiology*, 88(6), pp. 3421–3438. doi: 10.1152/jn.00194.2002.

Spellman, T., Rigotti, M., Ahmari, S. E., Fusi, S., Gogos, J. A. and Gordon, J. A. (2015) 'Hippocampal-prefrontal input supports spatial encoding in working memory', *Nature*, 522(7556), pp. 309–314. doi: 10.1038/nature14445.

Tønnesen, J. (2013) 'Optogenetic cell control in experimental models of neurological disorders', *Behavioural Brain Research*, 255, pp. 35–43. doi: 10.1016/j.bbr.2013.07.007.

Tremblay, S., Acker, L., Afraz, A., Albaugh, D. L., Amita, H., Andrei, A. R., Angelucci, A., Aschner, A., Balan, P. F., Basso, M. A., Benvenuti, G., Bohlen, M. O., Caiola, M. J., Calcedo, R., Cavanaugh, J., Chen, Y., Chen, S., Chernov, M. M., Clark, A. M., *et al.* (2020) 'An Open Resource for Non-human Primate Optogenetics', *Neuron*, pp. 1–16. doi: 10.1016/j.neuron.2020.09.027.

Vargo, S. M., Belloir, T., Kimukin, I., Ahmed, Z. and Griggs, D. (2023) 'Smart Dura : A monolithic optoelectrical surface array for neural interfacing with primate cortex', *EMBC NER*, 116464, pp. 2–6.

Watanabe, H., Sano, H., Chiken, S., Kobayashi, K., Fukata, Y., Fukata, M., Mushiake, H. and Nambu, A. (2020) 'Forelimb movements evoked by optogenetic stimulation of the macaque motor cortex', *Nature Communications*, 11(1), pp. 1–9. doi: 10.1038/s41467-020-16883-5.

Yang, X., Yao, C., Tian, T., Li, X., Yan, H., Wu, J., Li, H., Pei, L., Liu, D., Tian, Q., Zhu, L. Q. and Lu, Y. (2018) 'A novel mechanism of memory loss in Alzheimer's disease mice via the degeneration of entorhinal-CA1 synapses', *Molecular Psychiatry*, 23(2), pp. 199–210. doi: 10.1038/mp.2016.151.

Yao, Z. and Yazdan-Shahmorad, A. (2018) 'A Quantitative Model for Estimating the Scale of Photochemically Induced Ischemic Stroke', *Conf Proc IEEE Eng Med Biol Soc*. 2018/11/18, 2018(C), pp. 2744–2747. doi: 10.1109/EMBC.2018.8512880.

Yazdan-Shahmorad, A, Diaz-Botia, C., Hanson, T. L., Kharazia, V., Ledochowitsch, P., Maharbiz, M. M. and Sabes, P. N. (2016) 'A Large-Scale Interface for Optogenetic Stimulation and Recording in Nonhuman Primates', *Neuron*, 89(5), pp. 927–939. doi: 10.1016/j.neuron.2016.01.013.

Yazdan-Shahmorad, Azadeh, Diaz-Botia, C., Hanson, T. L., Kharazia, V., Ledochowitsch, P., Maharbiz, M. M. and Sabes, P. N. (2016) 'A Large-Scale Interface for Optogenetic Stimulation and Recording in Nonhuman Primates', *Neuron*, 89(5), pp. 927–939. doi: 10.1016/j.neuron.2016.01.013.

Yazdan-Shahmorad, A., Diaz-Botia, C., Hanson, T., Ledochowitsch, P., Maharabiz, M. M., Sabes, P. N., Maharbiz, M. M. and Sabes, P. N. (2015) 'Demonstration of a setup for chronic optogenetic stimulation and recording across cortical areas in non-human primates', *SPIE BiOS*, 9305(March 2015), p. 93052K. doi: 10.1117/12.2080405.

Yazdan-Shahmorad, A., Silversmith, D. B., Kharazia, V. and Sabes, P. N. (2018) 'Targeted cortical reorganization using optogenetics in non-human primates', *Elife*. 2018/05/29, 7, pp. 1–21. doi: 10.7554/eLife.31034.

Zaraza, D., Chernov, M., Friedman, R. M., Yang, Y., John, A., Zaraza, D., Chernov, M. M., Friedman, R. M., Yang, Y. and Rogers, J. A. (2020) 'Going wireless: an optical imaging and optogenetics system for use in awake behaving primates', 1122705(February). doi: 10.1117/12.2546289.

Zhou, A., Santacruz, S. R., Johnson, B. C., Alexandrov, G., Moin, A., Burghardt, F. L., Rabaey, J. M., Carmena, J. M. and Muller, R. (2019) 'A wireless and artefact-free 128-channel neuromodulation device for closed-loop stimulation and recording in non-human primates', *Nature Biomedical Engineering*, 3(1), pp. 15–26. doi: 10.1038/s41551-018-0323-x.

Zhou, J., Khateeb, K., Gala, A., Rahimi, M., Griggs, D. J., Ip, Z. and Yazdan-shahmorad, A. (2022) 'Neuroprotective Effects of Electrical Stimulation Following Ischemic Stroke in Non-Human Primates *', *IEEE EMBC*, 119395, pp. 1–4.

Zhou, J., Khateeb, K. and Yazdan-Shahmorad, A. (2023) 'Early Intervention with Electrical Stimulation Reduces Neural Damage After Stroke in Non-human Primates', *bioRxiv*, p. 2023.12.18.572235. doi: 10.1101/2023.12.18.572235.